

3. Experiment

A more in-depth discussion of the experimental procedure than found in the introduction is in order. A good understanding of the experimental procedure will allow the reader to evaluate the data with greater clarity, and repeat the experiments if necessary. In addition, experimental procedure is a type of technology. A successful procedure is not always obvious, and any information gained that could help other physicists in performing experiments is always of value. The experimental procedure used in the feed-out shots was based on previous successful experiments performed by other physicists found in the literature. A description of this previous work is documented in section 3.1. Section 3.2 describes the backlighter selection process, an important aspect of the experimental design. Section 3.3 reviews target fabrication procedures, whereas section 3.4 discusses target metrology. Fielding and diagnostics are covered in section 3.5.

3.1 Related Experimental Work by Others

By taking advantage of the experience of previous experimentalists, the feed-out campaign saved a great deal of time. Questions such as how much laser energy should be used on a Fe backlighter can only be determined by trial and error. The two sets of experiments described here had the configuration shown in Figure 1-5, with the exception that the perturbations were on the hot side, toward the hohlraum instead of on the cold side. Each experiment observed perturbation

growth from the Rayleigh-Taylor instability on planar foils and was performed at the NOVA laser facility. Schappert conducted experiments with copper [Schappert] whereas Remington's foils were plastic, CH(Br), and fluorosilicone, FS [Remington 1992, 1993]. Both used 527 nm green light for the backlighters and 351 nm blue light for the hohlraums.

Schappert performed experiments designed by Hollowell. The package was a 16 μm thick copper foil with a single mode, two-dimensional perturbation. Amplitudes of 0.4-0.5 μm and wavelengths of 45 and 80 μm were shot. Growth from the Rayleigh-Taylor instability was recorded using a microchannel plate and gated X-ray imager, which was believed to have a resolution less than 5 μm . They had difficulty seeing perturbations below 13 μm in wavelength. Side views were obtained with a streak camera, which had sub-picosecond temporal and less than 5 μm spatial resolution. The laser pulse shape was PS-26. The backlighter material and filter were both iron, which produced a very non-Planckian spectrum. The backlighter had intense lines at 6.7 and, to a lesser extent, 6.9 keV. The iron filter removed H-like lines, but allowed the He-like lines to pass through. Data was taken for 4 ns after the laser was fired. A strong second harmonic component was observed late in time.

The packages were modeled by Hollowell using 1-D LASNEX with the Takabe formula, Eq. (21), 2-D LASNEX, and 2-D RAGE. RAGE is a radiation-hydrodynamics code with single group radiation and an adaptive square mesh [Gittings, Byrne]. A non-Planckian source including the gold M-band radiation

was used. There was difficulty obtaining a good fit with the 1-D calculations, but the 2-D calculations matched the experimental growth rate reasonably well. RAGE 's square zoning simulated the perturbation in a stair-step fashion. At the beginning of the drive pulse, Hollowell found a jet of material emerging from each individual zone in the perturbation. The mode comprised of these jets appeared to couple with itself, producing a large second harmonic and matching the experimental results [Hollowell]. Although the jets were a computational artifact, something similar could have occurred in the experiment. The perturbation was machined into the copper in small steps of a similar size and shape as the square zones in RAGE. This high order perturbation could have coupled into the second as suggested by the code. Schappert hypothesized that the large second harmonic could also be a diagnostic artifact. Either insufficient camera resolution or an incorrect modulation transfer function could produce a spurious second harmonic, or portion of it. In late times, RAGE predicted a larger perturbation amplitude than observed. This discrepancy could have been due to the spikes being tilted at an angle to the camera.

Remington's experiments generated the hohlraum drive with a 3.2 ns shaped pulse and eight 2.1 kJ beams. The backlighter was a disk of Mo, Rh, Sc, or Fe. It was illuminated with a ninth NOVA beam with a wavelength, shape, and energy of 0.53 μm , 5.0 ns square, and 2.5 kJ respectively. There was concern that the backlighter structure might interfere with the experiment, so a random phase plate was used to smooth the beam's image on the disk. Remington used both

face and side-on radiography. Perturbation images with two spatial dimensions were obtained in face-on radiography using a gated X-ray pinhole camera. For side-on images, either a streaked 22X Woelter X-ray microscope, or a 20X magnification streaked-slit imager were used. Side-on diagnostics provided images with one spatial and one temporal dimension. The side-on view was important to verify foil acceleration, and face-on was used to observe the growth of instabilities.

Remington's experiments included single mode, two-mode, and multi-mode initial perturbations. For the single mode, a $100\text{ }\mu\text{m}$ wavelength initial perturbation with a $4.6\text{ }\mu\text{m}$ amplitude was placed on the foil. The single-mode evolved into the nonlinear bubble and spike formation after 4.4 ns , with the bubble growth asymptotically approaching that due to terminal velocity, and spike growth approaching that due to free-fall. There was a slight indication of foil bowing due to nonuniform drive from the hohlraum. For the two-mode case, wavelengths of 50 and $75\text{ }\mu\text{m}$ were used, and the coupled components of 30 and $150\text{ }\mu\text{m}$ were observed. The rough foil with random perturbations had a typical RMS deviation from the average of $1.7\text{ }\mu\text{m}$ whereas a smoother random foil showed only $0.1\text{ }\mu\text{m}$. The rough surface evolved after 4 ns into large, hexagonal bubbles of about $100\text{ }\mu\text{m}$ in transverse size, while the smooth foil showed no obvious perturbation growth.

Weber obtained good agreement between Remington's results and computational modeling using a time-dependent drive spectrum [Weber]. Non-LTE effects did not appear to be important.

3.2 Backlighter Selection

An important part of the experimental design process was to select an appropriate backlighter for each package. An unsuitable backlighter would mean low quality data, or no data at all. The first step to good data involves the creation of a monoenergetic source, which is desirable to simplify the data analysis and prediction, as one did not then have to be concerned with a time-dependent spectrum and different opacities for each component of that spectrum. Due to the highly ionized nature of the backlighter plasma, the majority of ions are stripped to the He-like state. The He- α transition was the line used in these experiments for backlighting and occurs in the singlet state of the He-like ions. Because the 2^1S state of the singlet is metastable, the He- α is a single line from the 2^1P to the 1^1S state. A particularly convenient aspect of the He-like transition energies is that they usually occur just before the K edge of the material. A cold filter of the same material as the backlighter will then filter energies above and below the He-like transitions, producing an approximately monoenergetic source. The ICF experimentalist selects a backlighter material by looking up the He- α transition energies of the elements. The element with the transition energy closest to the desirable energy for the experiment is then made into a backlighter disc.

There is a limited range of energies in acceptable backlighters. For high energies, above ~ 9 keV, the opacity is very low, and the X-rays no longer interact with the pinhole substrate in the X-ray camera strongly. The pinhole produces a

fuzzy image, and the resolution decreases. Below about 3 keV the spectrum becomes less monoenergetic. Another problem with using energies below 2 keV is that the package and target themselves are thermally radiating, which could lead to a confusing signal. For these reasons, only backlighters between 3 and 9 keV were considered.

An important concern in selecting a backlighter energy for face-on radiography is that the intensity be neither too large or too small. If the intensity reaching the film is too large, it will saturate, and if it is too small, no picture is recorded. Intensity is determined largely by material thickness and opacity. X-rays are attenuated as they pass through the package, according to

$$T = \frac{I(z)}{I_i} = e^{-\mu\rho z},$$

where I_i is the initial intensity, $I(z)$ is the intensity a distance z into the material, μ is the opacity and ρ the density of the material. T is the transmission ratio. The opacity is a function of X-ray energy and generally decreases exponentially with increasing energy. Thus, the higher the backlighter energy, the higher the transmitted intensity. The opacity can also be a strong function of material temperature for energies below about 3 keV. Above this energy, the cold, constant opacities were a reasonable assumption for the feed-out experiments. Intensity on the film increases with laser power on the backlighter and with the gain setting for the X-ray camera. Intensity decreases with increasing backlighter energy. As the Z number of the backlighter element increases, so does the energy of the He- α transition

and the energy associated with the He ionization state of the element. For very high energy lines, the He ionization state energy may become much higher than the thermal plasma energy. The relatively large ionization energy results in fewer ions to create the line, and a weaker signal.

Unfortunately, the intensity of the backlighter is almost impossible to calculate due to the non-LTE nature of the plasma and great number of ion states. Likewise, the response of the film and the effect of adjusting the gain of the camera are unpredictable. Generally, the higher the energy, the greater the intensity seen by the camera due to increased transmission, up to about 8-9 keV. The initial density and thickness of the package were often used for approximate transmission calculations. Transmission ratios of 5-20% seemed acceptable for the 4-7 keV backlighter energies used in the feed-out packages.

A second concern in the selection of backlighters for face-on radiography is that the intensity ratio of the perturbations be sufficiently large. As the backlighter X-rays passed through the peaks of the perturbations, they were attenuated more than those passing through the troughs. The cameras were capable of observing a ratio of these intensities of about 0.9, but generally lower intensity ratios were more desirable. If Z_{val} is the package thickness in the valleys, while Z_{pk} is the thickness through the peaks, then the intensity ratio, R , is given by

$$R = \frac{I_o e^{-\mu\rho Z_{pk}}}{I_o e^{-\mu\rho Z_{val}}} = e^{-\mu\rho\Delta z} \quad \Delta z = Z_{pk} - Z_{val}.$$

For an approximation at time zero, this ratio could be calculated using the initial conditions of the package. A much better estimate was made by using the TDG code, a LASNEX postprocessor, which produced contour plots of normalized intensity as a function of time. TDG used temperature-dependent opacities and density profiles from LASNEX. It also modeled the finite resolution of the camera, which decreases the observed intensity ratio. The backlighter was modeled as a spatially and temporally uniform monoenergetic source. The peak-to-valley intensity ratio could thus be plotted for a package versus time, given a specified backlighter energy. Such a calculation was conducted before each backlighter and package combination were fielded to make certain the perturbations were visible.

The intensity ratio decreases with opacity, which decreases with increasing X-ray energy. For a larger intensity ratio, one would thus go to lower energy backlighters. This experimental constraint is in competition with the desire for high intensity. There is usually a range of backlighter energies for which both of these constraints are satisfactorily met. However, one must be careful with material selection for the package. For a given package thickness, if the $\mu\rho$ product for the material were too low, to obtain a satisfactory intensity ratio, one might be forced to use a backlighter of such a low energy that there was almost no transmission. Likewise, if $\mu\rho$ were too high, to obtain adequate transmission, one would be forced to use an energy too high for a good intensity ratio.

The above discussion has been in regard to face-on radiography. Side-on radiography, will now be discussed as it has a different set of considerations. After the shock hits the perturbations on the rear surface of the package, material begins to move into the vacuum away from the package. A density gradient is established from the center of the package into the vacuum. The perturbations are usually located somewhere in this density gradient. The average density, size of the gradient, and location and size of the perturbation all change with time.

There is always some optimal X-ray intensity for imaging the package. X-rays passing through the low density or vacuum region will overexpose the film. X-rays passing through the center of the package will all be absorbed. Somewhere in between there will be a density contour that attenuates the backlighter line to just the optimal intensity for the camera. The hope is that this is the density contour containing the perturbation. As the target expands and density drops, the perturbation moves from high to low density contours. High energy backlighters penetrate higher density contours, and thus show earlier time history of the perturbation. Lower energy backlighters will follow the evolution of lower density contours, and see the perturbation at later times. Experimental uncertainties in such things as camera response and laser energy on the backlighter thus result in a diagnostic uncertainty as to which density contour is followed. This situation is unlike face-on radiography, for which experimental uncertainties determine if the package is observable.

Design of a side-on experiment is more difficult than face-on radiogra-

phy, as TDG can only predict relative intensity ratios. TDG was used to determine if the perturbations would be obscured too much by finite camera resolution. From the face-on experiments, it was known that certain combinations of backlighter energy and package thickness produced acceptable X-ray intensities. To find the density contour that the same energy backlighter would follow in a side-on shot, the intensity for sidelighting was equated to that for face-on, and solved for the side-on density contour, ρ_S . In the equation below, z_F is the package thickness for face-on experiments, whereas z_S is the thickness for side-on shots. As the package was 250 μm thick from the side, but only 35-85 μm when viewed from face-on, the sidelighting density was much lower than the initial density of the package

$$I_i e^{-\mu \rho_S z_S} = I_i e^{-\mu \rho z_F}$$

$$\rho_S = \frac{\rho z_F}{z_S}$$

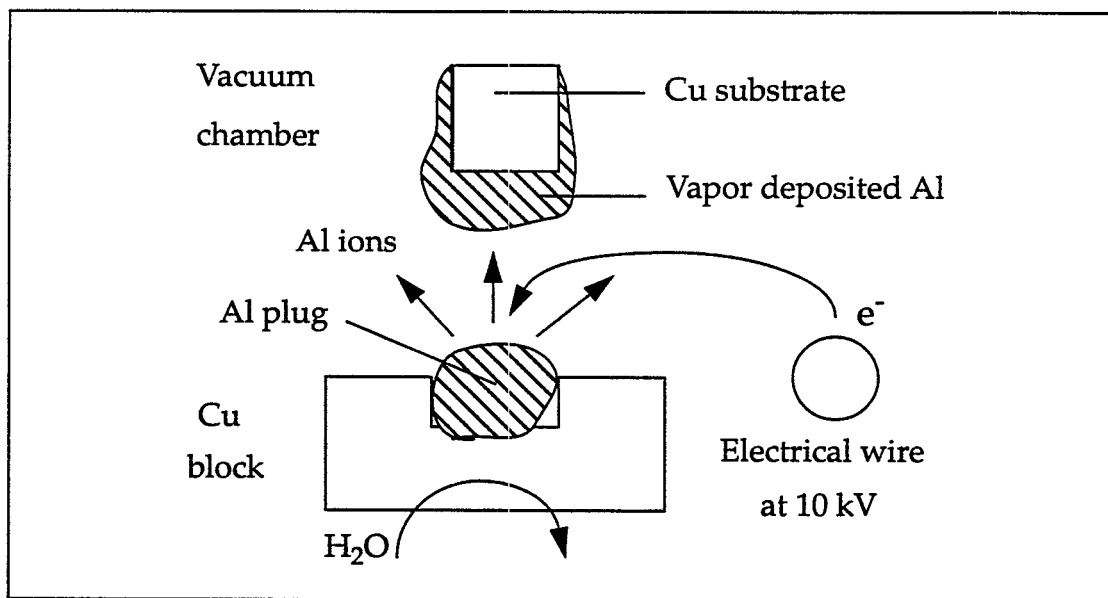
3.3 Target Fabrication

The creation of targets meeting the specifications of the experimental design was important to success, but it was not always easy. Because of the small number of targets used in the experiments, they were all made by hand. To fabricate the aluminum packages, a cylindrical copper substrate approximately 1 mm in diameter was placed on a lathe and machined flat. The substrate was then placed in a vacuum chamber and aluminum was vapor-deposited on the copper,

see Figure 3-1. To generate the vapor, a piece of aluminum was placed in an indentation in a copper block, which was biased 10 kV positive with respect to an electrical wire inside the chamber. Electrons were ejected from the wire and impacted the copper block and aluminum plug, causing aluminum ions to be ejected from the surface. To keep the aluminum from melting, water was circulated through the copper block. The copper substrate was positioned directly above and close to the aluminum plug, so as the aluminum ions were ejected, they were deposited on the substrate.

After a sufficient amount of aluminum was deposited, the substrate was placed back on the lathe and the aluminum machined flat to a thickness corresponding to the peak of the perturbations. The lathe was then used to cut a perturbation in the aluminum. The blade was not sharp enough to cut an exactly sinusoidal 50 μm wavelength perturbation, but it produced a good approxima-

Figure 3-1: Vapor Deposition of Al on Cu Substrate



tion. The edges were then cut off with the lathe so the package could easily fit on the hohlraum. The copper was dissolved with nitric acid, which does not react with aluminum.

To fabricate packages of aluminum with beryllium on the perturbed side, the copper substrate was machined flat on the lathe, then the sinusoidal perturbation was cut into the copper. The substrate was placed in the vacuum chamber with a plug of beryllium in the indentation of the copper block. Instead of electrons, argon ions were accelerated through an electric field into the beryllium. The beryllium was thus deposited on the copper. The beryllium and substrate were then placed on the lathe again and the beryllium machined to 10 μm thickness. This part of the procedure was difficult, as the beryllium would frequently flake off of the copper. To prevent this, it was important to have a very clean substrate before beryllium vapor deposition.

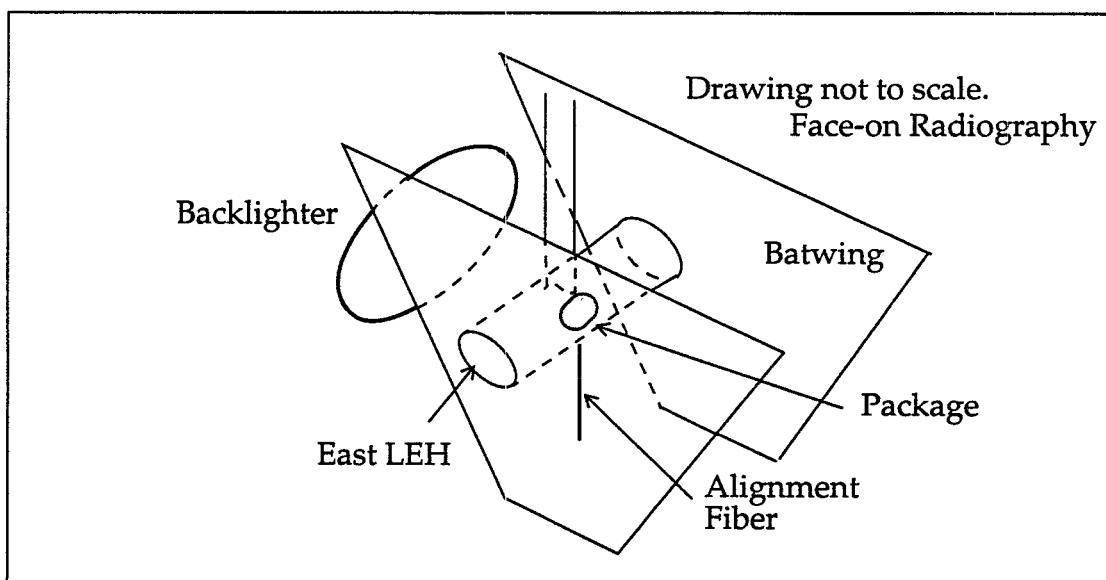
The beryllium and substrate were then placed back in the vacuum chamber and aluminum was vapor deposited on the beryllium. The aluminum was then machined flat to the desired thickness, and the copper dissolved with nitric acid.

Detailed drawings of the finished targets are shown in Figures 3-2 through 3-5B. The term LEH in these drawings refers to the "laser entrance holes" in the hohlraum. When the target is mounted in the NOVA target chamber, one LEH faces east, the other west. The terms east and west are therefore used to specify an individual LEH. The term SIM stands for "six inch manipulator." The SIM's

are ports in the laser target chamber for diagnostics.

The targets were composed of a package, hohlraum, backlighter, alignment fiber, and radiation shields. The alignment fiber was used to align the targets in the NOVA target chamber. There were multiple radiation shields. One was a gold shield used for face-on packages that was placed on the side of the hohlraum with a hole cut just large enough to view the package. Without this shield, radiation passing from the inside of the hohlraum would degrade the data. Two other shields, the batwings, were glued to the ends of the hohlraum. As hot plasma squirted out the ends of the hohlraum, these shields kept the radiation from the plasma from overexposing the X-ray film and ruining the data. The hohlraum, package, and shields were all glued together and to the end of a stalk coming up from a target stand. The backlighter was glued separately to another stalk attached to the same target stand. Small screws allowed fine adjustment of the

Figure 3-2: Hohlraum with Batwings



backlighter position.

Figure 3-3: Side View of Target Positioned in NOVA Target Chamber.

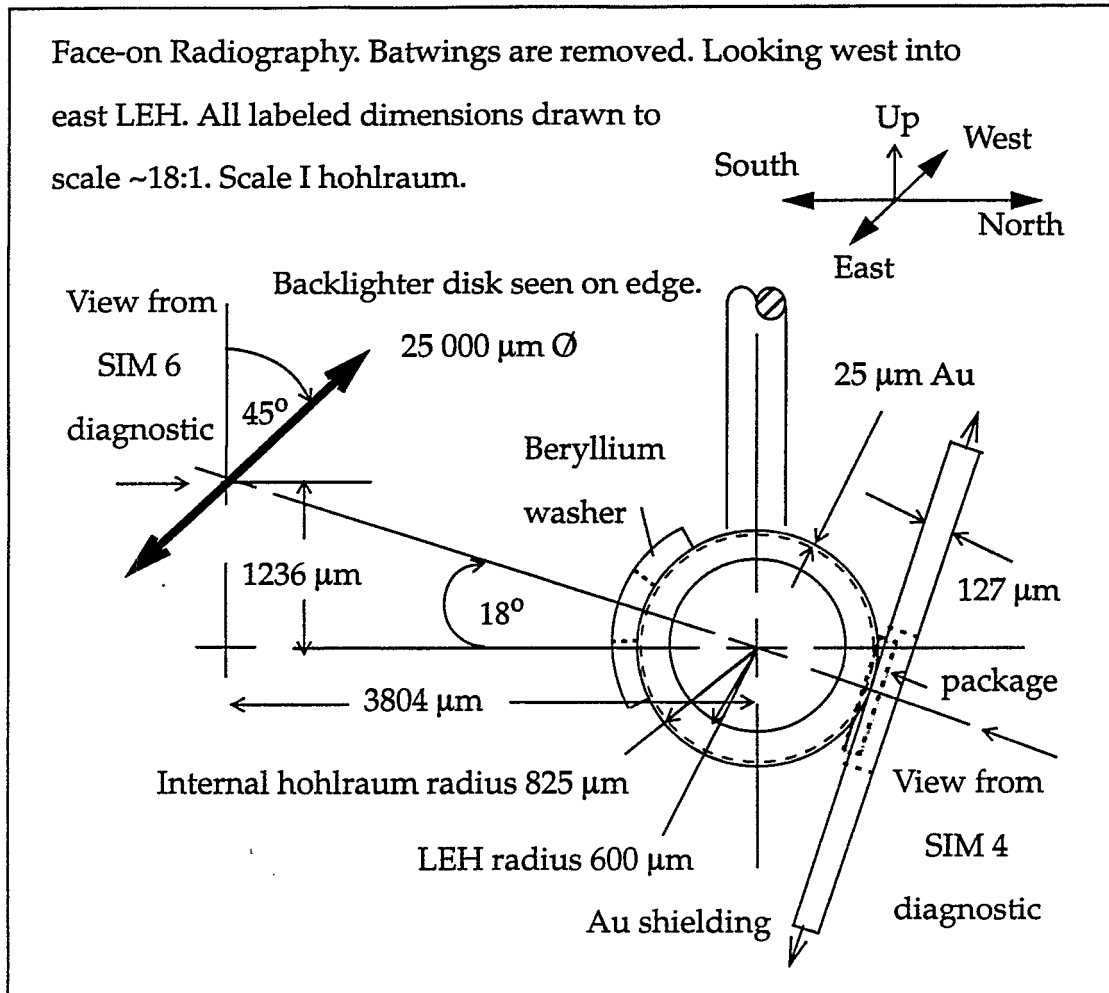


Figure 3-4: Additional Views of Face-on Radiography Target

Front view of target from SIM 4 position with Au shield and batwings removed. SIM 4 is 18° below the horizontal and to the north of the target.

All labeled dimensions drawn to scale $\sim 23:1$.

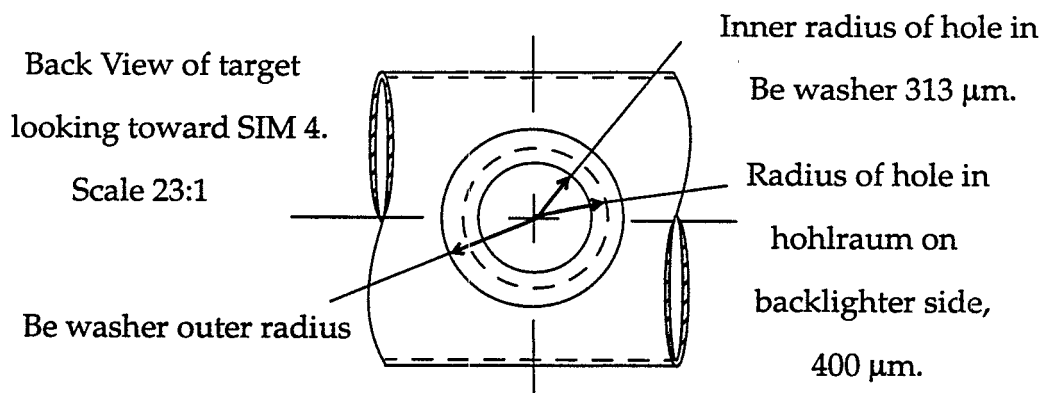
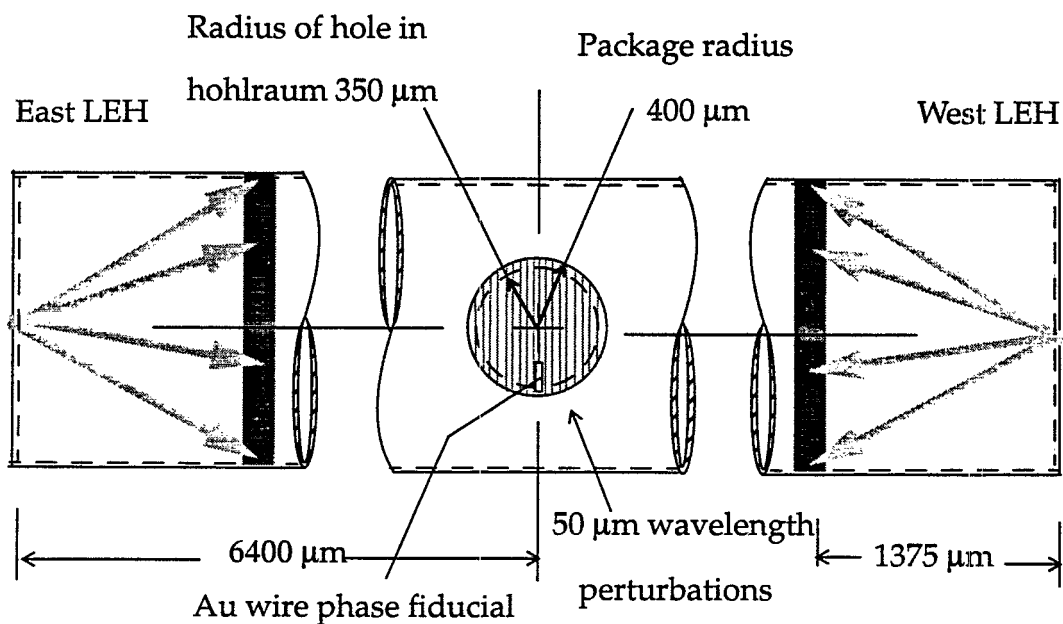


Figure 3-5A: Side-on Radiography

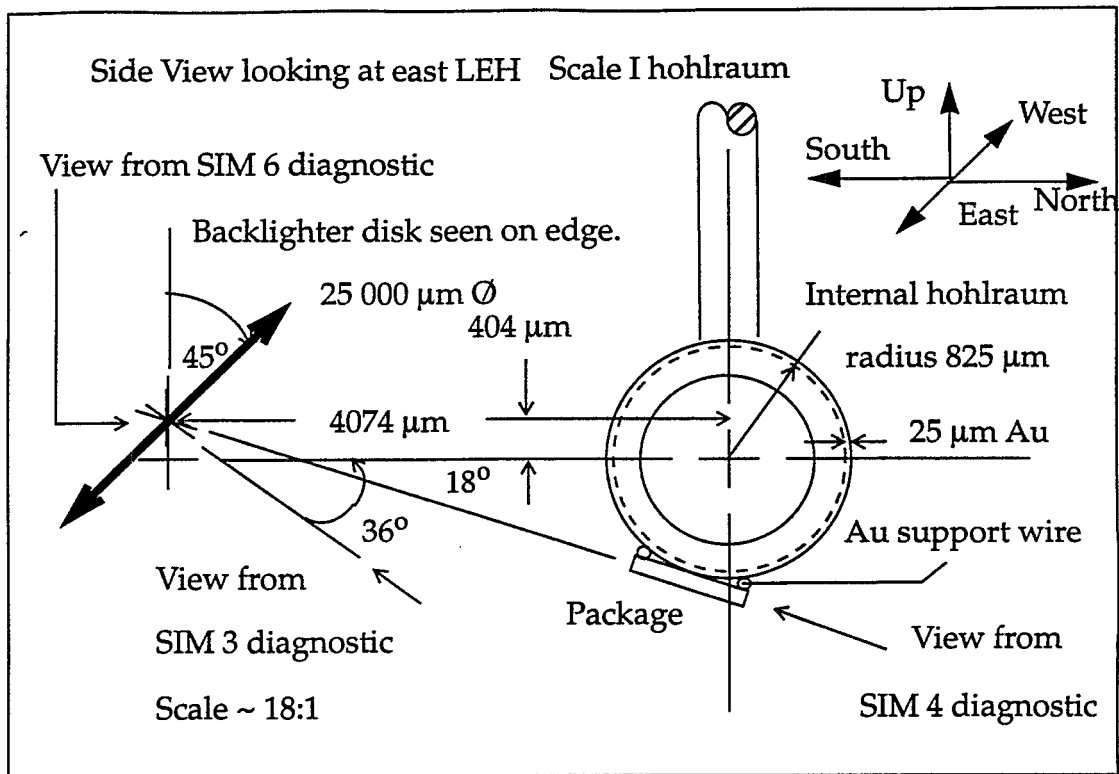
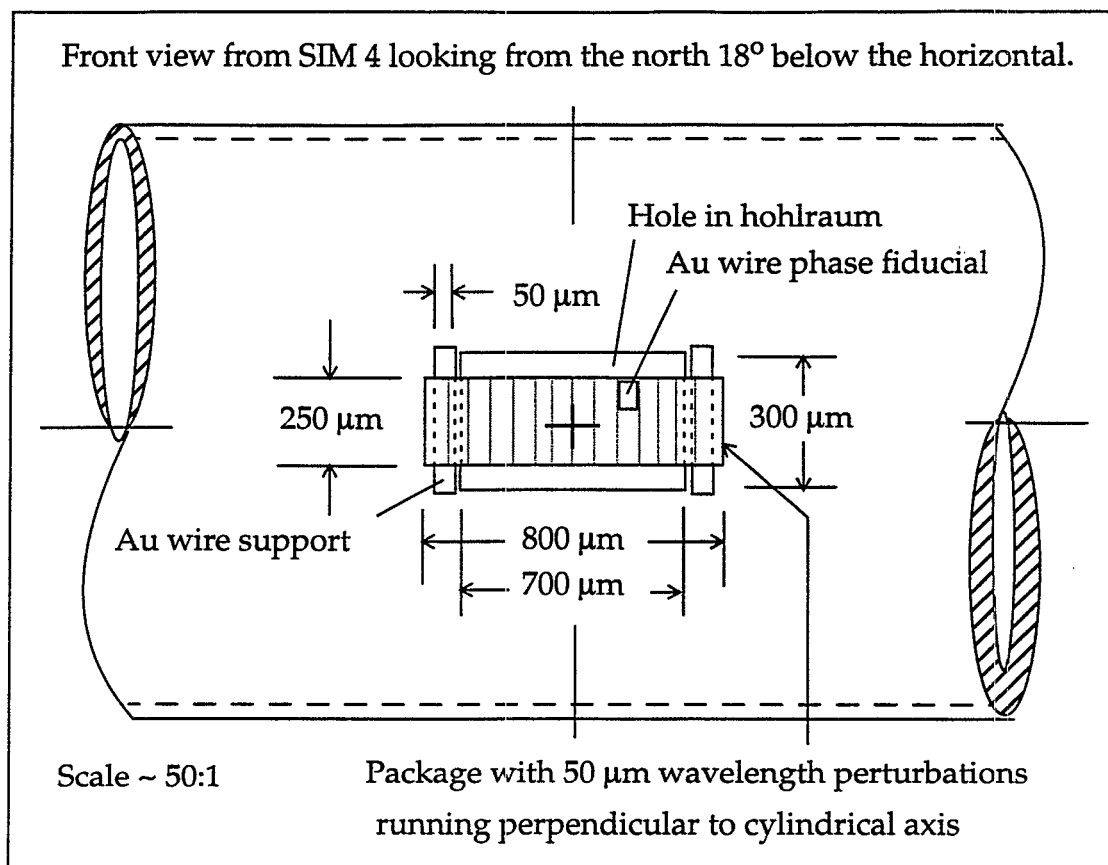


Figure 3-5B: Side-on Radiography



3.4 Target Metrology

The day before the shots were taken, all targets were metrologized at Lawrence Livermore National Laboratory. In metrologizing the targets, one made certain that they were of a sufficient quality to render good data. Metrology allowed one to determine if the errors in angle and position of the fixed parts were acceptable, and to adjust the parts that were still movable to their optimal positions. Defects could sometimes be corrected on site, and pictures were always

taken of the targets.

The metrology station consisted of a target manipulator accurate to a micron, computer software to control the manipulator, and a television screen connected to a camera and microscope for target viewing. Cross hairs on the television screen aided the work.

NOVA target chamber directions were used as reference positions on the metrology station. The target was initially positioned on the station with the operator facing the east LEH. The target could be moved up and down along the "y -axis", right and left along the "x -axis", and rotated at an angle α around the y -axis. The first task was to adjust α such that the metrology station camera was looking in a line of sight parallel to the hohlraum axis. This was accomplished by first positioning the cross hairs on the far left hand side of the east LEH. The camera was then alternately focused on the east and west LEH's. The x and α coordinates were iteratively adjusted until the cross hairs rested exactly on the far left hand side of both LEH's, indicating that the hohlraum was parallel with the line of sight. The center of the LEH was then found by measuring from one side to the next and dividing by two. LEH diameters were usually within about 10 μm of the expected measure. By moving to the top or bottom edge of the hohlraum and alternately focusing on the east and west LEH's, one could obtain an estimate of how much the hohlraum axis deviated from the horizontal.

The cross hairs were next positioned at the center of the east LEH again, and the three coordinates were zeroed. The coordinates for the backlighter posi-

tion were typed in. The backlighter was then moved to its optimal position by adjusting it until a small hole in the center of the disk was intersected by cross hairs on the television screen.

The target was rotated to the SIM 4 diagnostic view, showing the perturbed side of the package for face-on targets, and the side view for side-on targets. The center of the package was found and the x coordinate recorded. The target was then moved along the y -axis until the alignment fiber was observed. The deviation of the fiber from package center was noted and used to better position the target in the laser chamber. It would have been preferable to measure deviation from hohlraum center, but this was not possible with the batwings attached.

Remembering the x coordinate for package center, the target was rotated 180° , revealing the rear surface of the backlighter. The disk was then adjusted until the hole in its center was positioned at the x coordinate for package center. Next the target was rotated to show the backlighter disk as seen by the two backlighter beams. If the beam paths were obscured by the batwings, the batwings were clipped. Lastly, the target was rotated to display the package edge on, and package thickness was estimated. Estimates of package thickness not be made in the targets with gold shielding, because the shielding obscured the package.

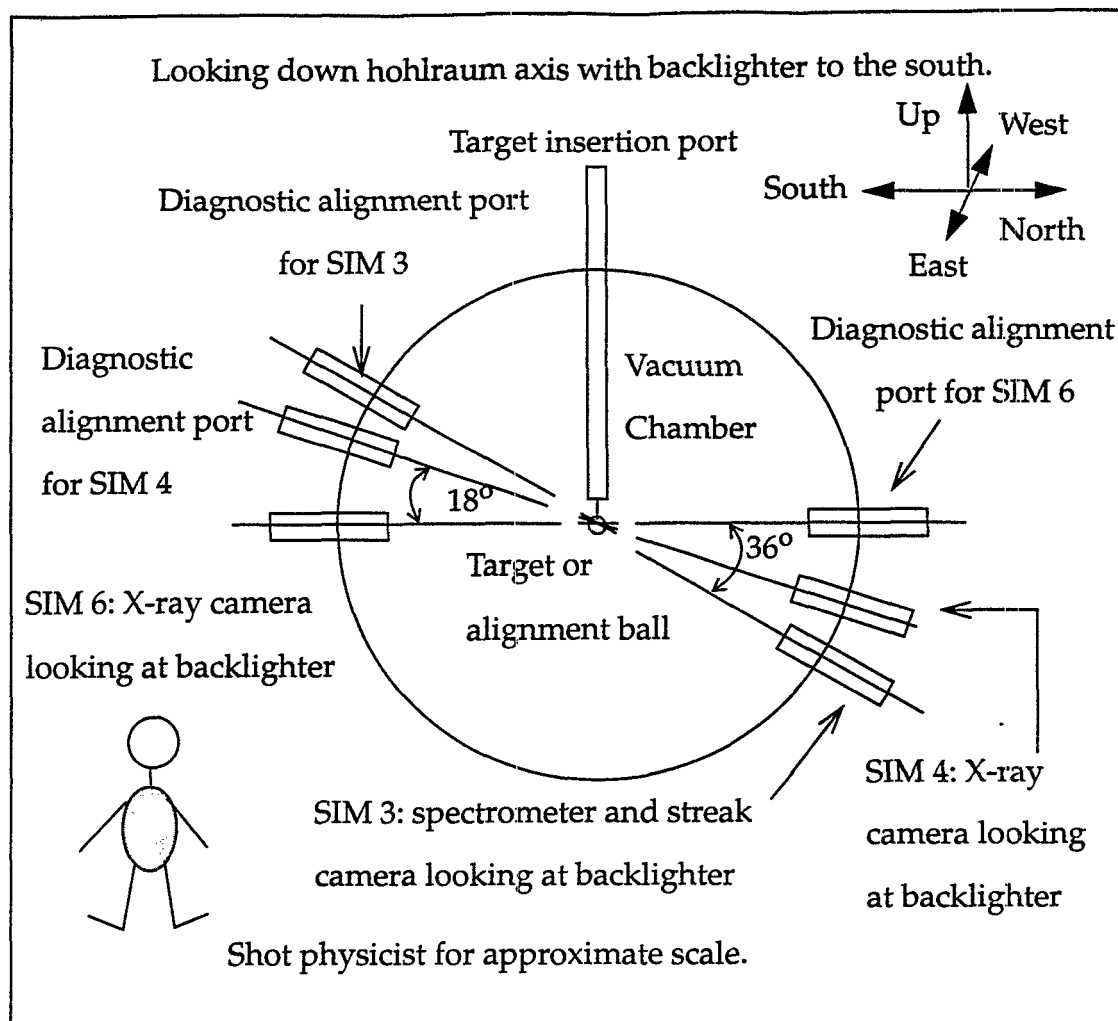
3.5 Target Fielding and Diagnostics

The first step in fielding the targets was to provide NOVA technicians with a list of experimental details before each shot. These documents were termed set-up sheets, and provided information such as which diagnostics to use in which SIM, laser energy, diagnostic pointings, and so forth.

The X-ray camera looking at the package was placed in SIM 4, the streak camera looking at the backlighter in SIM 3, and the X-ray camera observing the backlighter in SIM 6, see Figure 3-6. Each port had small hand-turned cranks with which to adjust the viewing angle. To align the diagnostics, an alignment ball was placed in the chamber where the target would be. View ports, referred to as "target alignment viewers," or TAV's, were located directly opposite each of the diagnostic ports. Each TAV contained a telescope looking back along the line of sight of the opposing SIM. The shot physicist looked through a telescope while directing a technician in the adjustment of the diagnostic in the opposite SIM. Adjustments were made until the alignment ball was in the center of the snout of the diagnostic, as observed with the telescope.

The target was positioned in the chamber from the NOVA control room using the alignment fiber and the fibers' recorded deviation from package center measured in metrology. The two backlighter beams were turned on at very low power, and the beams adjusted so each laser spot was positioned correctly on the backlighter disk. Green light with a 527 nm wavelength was used for the two

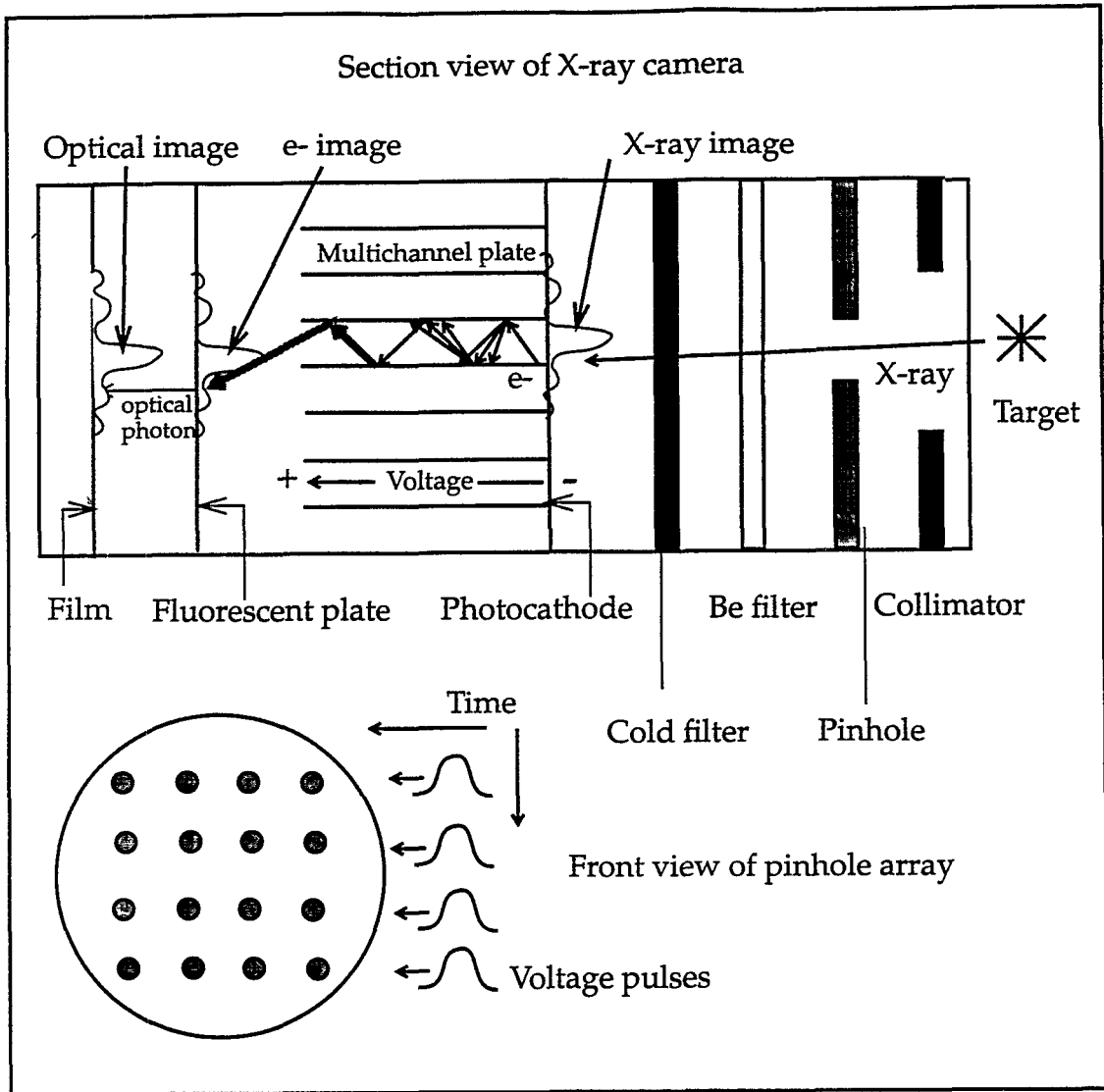
Figure 3-6: Section View of the NOVA Target Chamber



backlighter beams, whereas blue light at 351 nm was used in the hohlraum. Using two of NOVA's ten beams for backlighting caused the remaining eight beams to form an asymmetric ring of laser spots inside the hohlraum. This radiation asymmetry is not believed to have interfered with the experimental results.

Two types of X-ray cameras were used in the experiments, GXI's, or gated X-ray imagers, and FXI's, or fast X-ray imagers. There was no difference in the basic design of the cameras. The FXI was a commercially manufactured

Figure 3-7: Operation of X-ray Camera



machine whereas the GXI was built at the laboratory.

Figure 3-7 shows camera operation. X-rays from the target passed through a collimator, pinhole array, beryllium filter, and a cold filter, before forming an image on the microchannel plate.

The collimator was composed of 250 μm diameter holes, bored into a 75

μm thick substrate. For some of the experiments, an additional collimator of 50 μm diameter holes was also used. The pinholes were 5-10 μm in diameter and cut in a 75 μm substrate. There were sixteen collimator holes and pinholes each in a four by four array. Each collimator hole was directly above a pinhole.

The beryllium filter protected the camera from debris as well as acting as a low energy X-ray filter for energies less than about one keV, including the thermal hohlraum spectrum. The cold filter was of the same material as the backlighter and was referred to as cold because room temperature opacity tables could be used to predict its attenuation of the X-rays. The cold filter helped produce a very monoenergetic backlighter.

Behind each pinhole was a photocathode and microchannel plate, composed of millions of tiny tubes, arranged in a honeycomb fashion as viewed from the pinhole. After passing through the pinhole and filters, the X-rays formed an image on the photocathode. An individual X-ray from the image would strike the surface of the photocathode, generating an electron by the photoelectric effect. The electron would then be accelerated down a tube in the microchannel plate, creating a cascade of electrons as it interacted with the wall. The process was similar to how a photomultiplier functions. At the end of the tube, the electron cascade struck a fluorescent material, emitting a flash of light, which was recorded by the film. The voltage in the microchannel plate could be adjusted, thus changing the gain of the camera to be more or less sensitive to X-rays.

Four pinholes in a line in the array were referred to as a strip. A timing

delay could be set between the firing of the four strips, but no timing delay could be set between individual pinholes on the same strip. When a strip was fired, a voltage pulse would run down the strip, energizing each microchannel plate as it passed. Individual microchannel plates were only active during the time the voltage pulse was passing, and not after. The microchannel plates were active for about 80 ps each, during which time the image was formed on the film. Thus, if a process was shorter than 80 ps, there would be some blurring, but this was not a problem for the feed-out experiments. The total time for a pulse to run across a strip was about 250 ps, so there was some temporal overlap in the images.

A single timing pulse from the NOVA control room was sent well in advance of the laser pulse to trigger the diagnostics. Each diagnostics defined the beginning of the experiment as the time at which it received the timing pulse. Just before the pulse from the control room reached a diagnostic, it entered a delay box for that diagnostic. The delay box added just the right amount of delay in order for the diagnostic to receive the timing pulse exactly at the beginning of the experiment. There was a different delay from the control room to each diagnostic due to differences such as cable length, and so each delay box had to be set to a different delay. In this way, all the diagnostics and the laser were fired simultaneously. The correct delays for each diagnostic were posted on the delay boxes. These delays were dialed in before each shot.

The initial timing pulse was broken into four pulses when it reached the camera, with each one being delayed somewhat with respect to the previous

one. The first strip could be delayed for many nanoseconds from $t=0$. The succeeding three strips could be fired at a minimum of 250 ps apart, which resulted in a little overlap, or as much as 750 ps apart. Whenever two identical shots were taken, the strip timings were staggered so each shot covered the total temporal range of interest, against the possibility that one of the shots would not yield data.

The X-ray camera snouts were placed about 30 mm away from the target, providing a magnification of twelve times. For a pinhole camera, magnification is simply the ratio of the distance from the image to the pinhole, divided by the distance from the object to the pinhole.

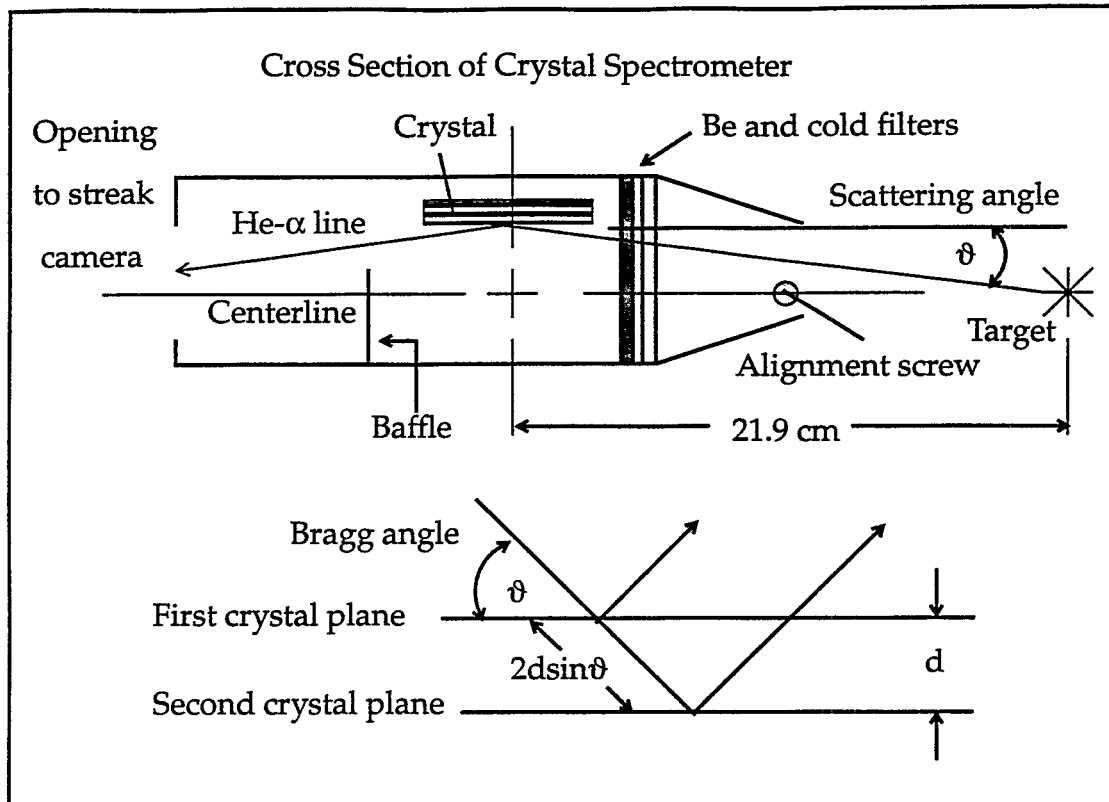
The backlighter spectrum was recorded on each shot using a spectrometer and streak camera, see Figure 3-8. X-rays from the backlighter scattered off a crystal in the spectrometer and into the camera. Different frequencies were scattered at different angles, so the streak camera saw a spectrum. For each frequency there is an angle, its Bragg angle, for which X-rays scattered off two different crystal planes will constructively interfere. This angle is given by

$$n\lambda = 2d \sin \vartheta ,$$

where n is the order of reflection, and indicates whether the scattering planes are the first and second, $n=1$, first and third, $n=2$, and so forth; d is the distance between planes, and ϑ is the scattering angle.

The spectrometer was aligned with the target using a screw that was on the snout and designated the centerline. The position of the crystal was adjusted such that when the He- α line from the backlighter scattered off the center of the

Figure 3-8: Bragg Angle and Section View of Crystal Spectrometer



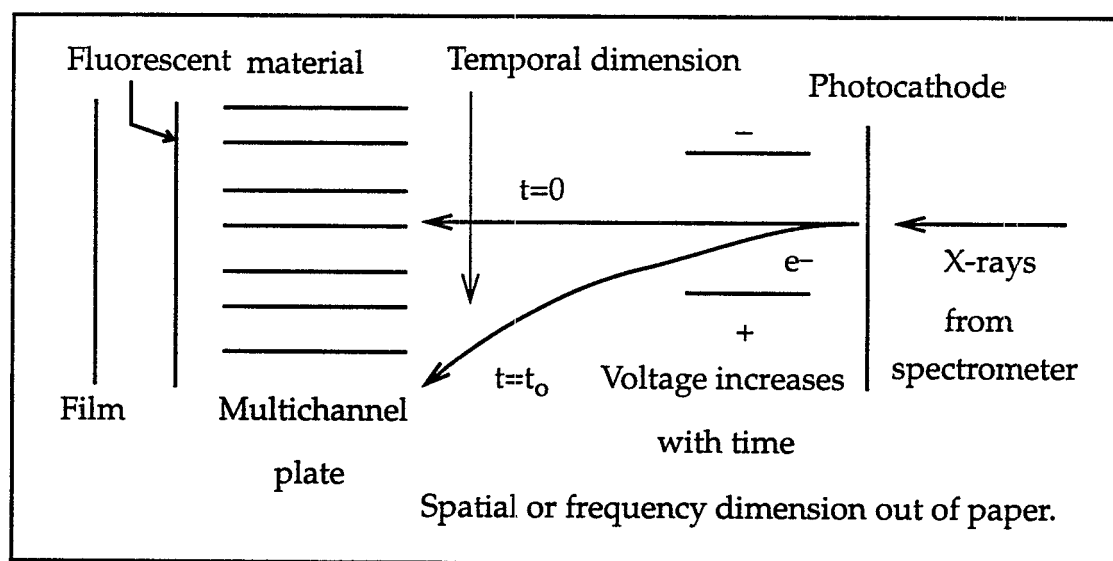
crystal, it was centered on the opening into the streak camera. First order reflection was always assumed. Two crystals were used in the experiments. For energies above 6 keV, a rubidium acid phthalate (RbAP) crystal was used, which had a $2d$ spacing of 26.121 Å. For the lower energy backlighter, a pentaerythritol (PET) crystal with a 8.742 Å $2d$ spacing was used. Baffles in the spectrometer prevented the X-rays from directly interacting with the streak camera, and a beryllium filter in the front prevented optical and lower frequency X-rays from interfering with the diagnostic as well as protecting the crystal from debris.

A streak camera is made to generate a picture with one dimension in

space, and the other in time, see Figure 3-9. The temporal resolution is less than a picosecond, while the spatial resolution is on the order of $5\text{ }\mu\text{m}$. X-rays from the spectrometer strike a photocathode, changing them into electrons. They drift through an electric field perpendicular to their motion and enter a multichannel plate. The electric field is generated by placing a voltage across two plates. The voltage is swept from a low to high value during the experiment and moves the electron image of the X-ray spectrum from the top to the bottom of the multichannel plate as it does so. The multichannel plate is similar to the one found in the GXI and FXI described above. The electrons emerge on a fluorescent plate, which converts them to optical photons, recorded on film.

There was some concern that the perturbation growth observed in the experiments was due to factors other than the machined perturbations. Target imperfections or drive asymmetry could be seeding the growth. To answer this

Figure 3-9: Streak Camera Operation



question, one shot was made with no initial perturbation. A Fourier analysis of the results was performed, and the part of the spectrum corresponding to the first harmonic in the perturbed packages observed. The first harmonic frequency showed a random fluctuation around a small initial value corresponding to a perturbation with a $\Delta\rho z$ of $5.59(10^{-4}) \pm 2.97(10^{-4}) \text{ g/cm}^2$. The symbol $\Delta\rho z$ is a measure of the size of a perturbation and is defined as the difference between the integral of density along a line running through the perturbation peak and a line running through the perturbation valley,

$$\Delta\rho z = \int_{\text{peak}} \rho(z)dz - \int_{\text{valley}} \rho(z)dz$$

This shot also yielded an experimental error estimate of $\pm 0.3 \text{ g/cm}^2$ for the $\Delta\rho z$ of the packages with machined perturbations.

Some data analysis was required after the experiments were performed. The side-on data was only qualitatively compared to calculations, but the face-on Fourier spectrum was directly compared to computational results. To determine the spectrum from the data took several steps. The strips of film from the X-ray camera were digitized at NOVA and mailed to Los Alamos. The film did not darken linearly with light intensity, so the film response function had to be determined. In addition to the time history of a package, on each strip there was a "wedge" created by a uniform light source shining on the film through a filter. The filter was transparent at one end and gradually became completely opaque on the other. By performing a spline fit to the wedge, one could obtain the film

response function.

An image of the package at a particular time was then selected. The average intensity of all the pixels around each individual pixel in the image was calculated. If the intensity of the central pixel deviated by more than a factor of 20 from the average, its intensity was set to the average, which helped to correct for defects in the film. The image was then corrected for film response, producing pixel intensities directly proportional to exposure.

Exposure was plotted along a line running perpendicular to the perturbations, producing what is called a lineout. The lineout had a long wavelength component due to variations in the backlighter intensity with position. The long wavelength was removed so the average value of the lineout function was zero. The natural log of the lineout was taken, and a Fourier transform was performed on the result. A cosine filter was used to eliminate high frequencies. There was usually some broadening of the harmonics around their central frequencies due to finite diagnostic resolution and the use of various filters, and possibly the physics. The amplitudes of these sidebands were added to that of the central harmonics. These values were divided by the modulation transfer function of the camera and compared to the calculations.

4. Computation with LASNEX

LASNEX is a two-dimensional, cylindrical, Lagrangian radiation-hydrodynamics code used primarily for modeling ICF plasmas [Zimmerman]. Runs are set up and controlled using a generator deck, a file created by the user with FORTRAN like commands for the main code. To run a planar calculation, such as for feed-out, one must place the package radially far away from the origin to minimize geometric cylindrical effects. The finite difference equations of hydrodynamics are solved directly, which is known as direct numerical simulation. Historically, this has not always been the case with hydrodynamics calculations, with perturbation growth being modeled by simple formulas on top of a zeroth-order hydrodynamics calculation. Partial pressures due to plasma components such as the ions, electrons, and photons are included in the hydrodynamics. The zoning is quadrilateral, with \bar{z} and \bar{r} , components.

Because the code is Lagrangian, the mesh often becomes distorted. A remapping subroutine was used for the thin packages to allow the calculation to continue past mesh tangling. Comparisons of remapped calculations to pure Lagrangian for the thin packages showed little deviation up to mesh tangling, after which the remapper gave a more realistic answer.

Attempts were made to increase the speed of the calculation by “feathering” the zoning. In other words, increasing the thickness of each zone by a small factor, progressing from the initial perturbation to the ablation surface. These calculations produced incorrect results. It was found necessary to zone the ablation

region as finely as the perturbation to obtain a correct answer.

In general, one needs finer radial zoning to resolve higher harmonics. For all but the thick packages, 45 radial zones were used in order to resolve down to the third harmonic. Convergence studies on the radial zoning indicated that this was sufficient. For the thick packages, 12 radial zones were used. Both Fourier analysis of these calculations and experimental data implied only a fundamental mode, so calculations with a better radial resolution were not pursued. Almost all of the calculations were run with a half-wavelength and reflective boundary conditions to save computer time. The zones were usually mass matched across the aluminum/beryllium interface to minimize the shock reflecting off of the mesh at this point. Some calculations were performed without radiation, where the shock was generated with a pressure source instead. These calculations had to have square root of density matching across the aluminum/beryllium interface for the code to function properly.

The perturbation was generated in the mesh by slowly increasing the thickness of the zones as one moved from the bottom to the top of the package. Only the last 5 μm of the mesh was perturbed. In hind-sight, this probably produced some computational error as the shock passed. In the thin target calculations, the remapper was turned on before shock arrival, so the shock interacted with a predominately square mesh.

The material surrounding the package was given a density several orders of magnitude below the package, to prevent it from interfering with the

calculation or radiation delivery to the ablation surface. The low density of this material also contributed to mesh tangles. Edges of the mesh were placed far enough away from the package so shocks in the low density material did not strike the boundaries during the calculation, which increased computational speed.

Equations of state were calculated and tabulated by a group at Los Alamos specializing in the physics. The user specified the material in each region of the calculation and the corresponding equation of state to be used. LASNEX does not have strength of materials, and considers everything a fluid. Modeling of the packages in very early time going from solid to plasma, and in-between, is not done correctly.

LASNEX assumes thermal electrons to have a Maxwellian distribution. Transport of the electrons is accomplished with tensorial plasma conductivities in a magnetic field, modified by a flux limiter and variable degree of ionization. Thermal ions are heated by Coulomb collisions with the thermal electrons and by hydrodynamic compression. The Saha equation is used to determine the population of various charge species.

LASNEX is capable of modeling interaction of laser light with the hohlraum, the generation of X-rays, and interaction of the hohlraum spectrum with the capsule simultaneously. Modeling all of these processes simultaneously is referred to as an integrated calculation and is computationally intensive. For feed-out package simulations, a much simpler approach was taken. A time dependent

hohlraum spectrum was written in the generator deck that ran LASNEX. This spectrum was then used to drive the feed-out packages. For PS-35, only an experimentally determined hohlraum temperature as a function of time was available, so a Planckian source was used. Hohlraum spectrums normally contain a large gold M-band component of X-rays, greater than 2.5 keV, which is non-Planckian. The lack of data on the PS-35 M-band caused some error in the computational modeling of package preheat. The PS-26 spectrum had been determined both by experiments and computation and included the M-band component.

Opacities, like the equation of state, were calculated and tabulated by a group at Los Alamos specializing in opacity physics. Although LASNEX has the capability to calculate its own opacities, these are believed to be inferior to the tabulated values. LASNEX opacities were only used to model the thick packages and seemed to generate a satisfactory result for these two cases. Tabulated opacities were used in all the other calculations.

To use the tables, the user creates an opacity file from them by specifying the desired mix of materials for each region and the binning. The radiation conservation equation is solved using a multi-group, flux-limited diffusion approach, with the groups being the user-specified opacity bins. Redistribution of photon energy due to Compton scattering is treated using a Fokker-Planck approximation.

To model feed-out packages, the binning ran from 30 eV up to 50 keV. Below 30 eV, the frequency was close to the plasma frequency, and the radiation

was totally absorbed. The hohlraum temperature was between 100-200 eV. Sufficiently refined binning below the K edge of aluminum, 1.56 keV, was important to correctly model the shocks and ablation region, while the bins above the K edge contributed mostly to preheat. Because of the low opacity of beryllium, it was not a consideration in binning. For the energies above the aluminum K edge, a standard diffusion model would be a poor representation, as the radiation has little interaction with the material and is very non-isotropic. The flux-limiting aspect of the LASNEX model should have compensated for this to some degree. Feed-out calculations were run assuming LTE, as a few non-LTE calculations did not reveal a substantial difference in the results. In hind-sight, the binning would have been better if consideration had been given to the radiation source binning in the LASNEX generator deck.

The first attempt at radiation binning involved the derivation of a simple equation describing the rate of energy exchange between the plasma and radiation field. Bins were then selected such that each represented the same rate of energy exchange on the average. Binning in this way did not succeed. The great majority of energy exchange was occurring close to the hohlraum temperature, so the binning was very tight around 200 eV, and unacceptably large over 600 eV. In response to this problem, logarithmic binning was adopted. Convergence studies were run for logarithmic binning above and below the aluminum K edge. The binning was found to have a strong effect on the shock strength. Acceptable convergence occurred with 20 bins below and 40 bins above the aluminum K edge.

5. Computational and Experimental Results

Feed-out is a process by which a perturbation on the cold surface of a radiatively driven foil is hydrodynamically communicated to the ablation surface, seeds the Rayleigh-Taylor instability there and grows. The hydrodynamic signal that communicates the perturbation from the cold to the hot surface is referred to in this chapter as the “seed.” As long as the foil is thick enough, the Rayleigh-Taylor and Richtmyer-Meshkov instabilities are independent, but as the radiation burns through the foil and the perturbations grow, they begin to interact. It is important to distinguish that this is a two step process. The perturbation feeds-out, grows, and feeds-back in. The entire process is collectively and loosely called “feed-out” here.

The feed-out process is important in the study of ICF capsule physics because it connects the large internal perturbations on the DT ice with the strong, long-lived Rayleigh-Taylor instability on the ablation surface. A reduction of feed-out is hypothesized to be responsible for the superiority of beryllium over plastic NIF capsules because of the additional thickness of the beryllium near the end of the pulse, and because of the larger density jump from the ice to the ablator. To study the effect thickness and density jump have on feed-out, calculations and experiments were performed and compared.

The reader is first presented with a brief review of how the data was obtained and considerations on how to best interpret the results presented here. Next, three fundamentally different feed-out situations in regard to thickness are

discussed. The thick foil situation with little coupling between the cold and hot interfaces, the thin foil case with strong coupling, and the intermediate case which moves from weak to strong coupling during the shot. The first two cases are used to suggest that feed-out to the ablation surface is weakened as thickness increases. The latter case is instrumental in demonstrating that feed-in of the perturbation from the hot to the cold surface is inhibited by foil thickness.

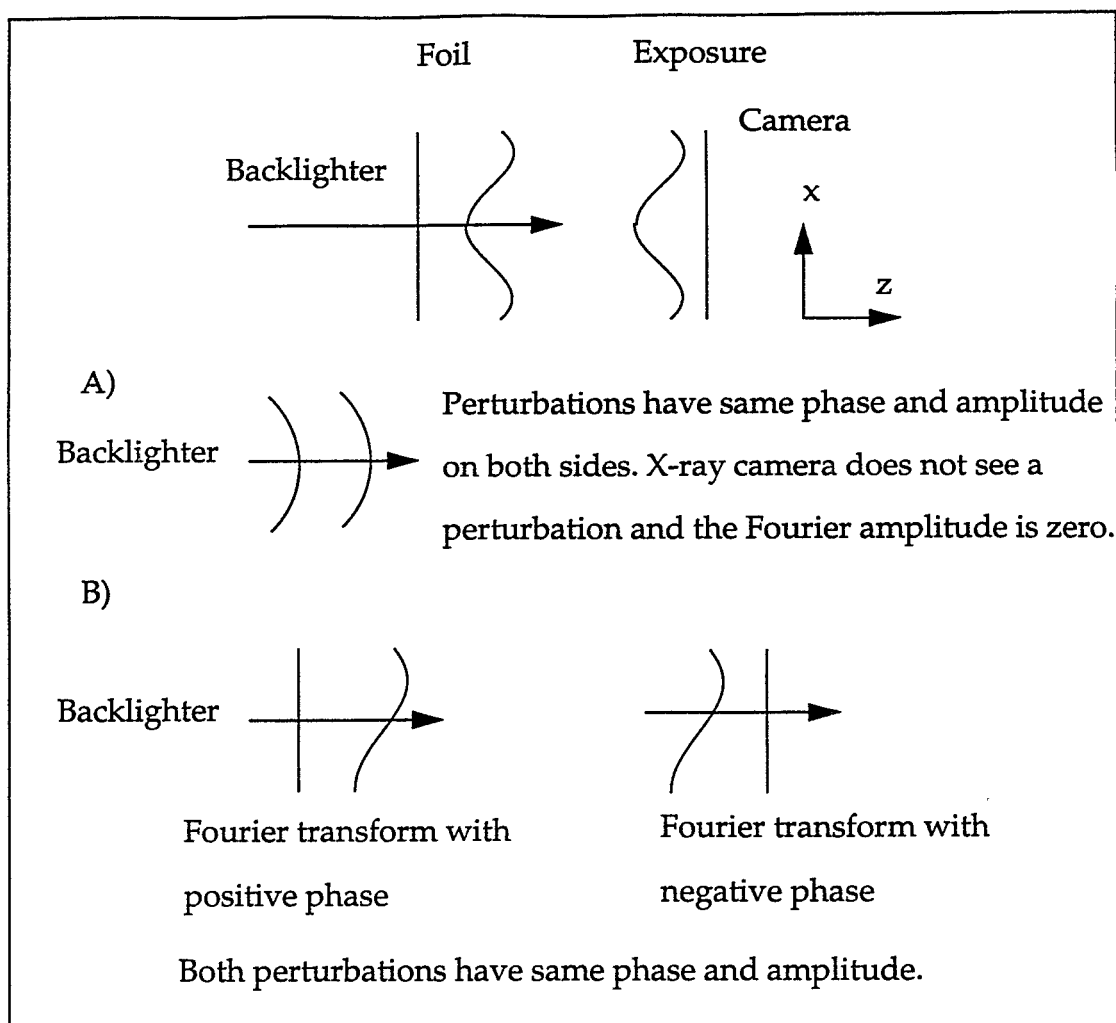
There will then follow a discussion of computational and experimental evidence indicating that a density jump may have some effect on feed-out, but the effect is probably not large. Lastly, three interesting items will be reviewed which were learned during the course of the project, but may not be directly related to feed-out.

The majority of the data presented here is from face-on radiography and was Fourier analyzed to show modal structure. The Fourier amplitudes show how the perturbations grew and coupled. Exposure versus position data, see Figure 5-1, was first normalized for a specific time, then converted to attenuation versus position by taking the natural log of exposure. Attenuation is defined here as the integral of opacity, μ , and density, ρ , along the path of the backlighter X-rays, $\int \mu \rho dz$. The attenuation versus position curve was Fourier transformed at different times in the experiment. Amplitudes of the various harmonics were then plotted against time. Because the data was normalized, the Fourier amplitudes are dimensionless. To compare with the data, LASNEX calculations were postprocessed using TDG to simulate diagnostic results. Both computational and experi-

mental data are plotted in the figures that follow. In all the plots the open symbols with lines drawn through them, circles, bow ties, and triangles, are the TDG results and represent the first, second and third harmonics respectively. The closed symbols are experimental data. Error bars in the Fourier amplitude of all the data points are shown but are based solely on null shot data. There were many other factors contributing to experimental error including uncertainties in foil thickness and variations in the laser energy and pulse shape. Some of the experimental variations are recorded in the appendix. The reader should also keep in mind that there is an estimated 500 ps timing error on all points which is not shown to make the plots more readable. The noise level of each experiment is recorded on the graphs.

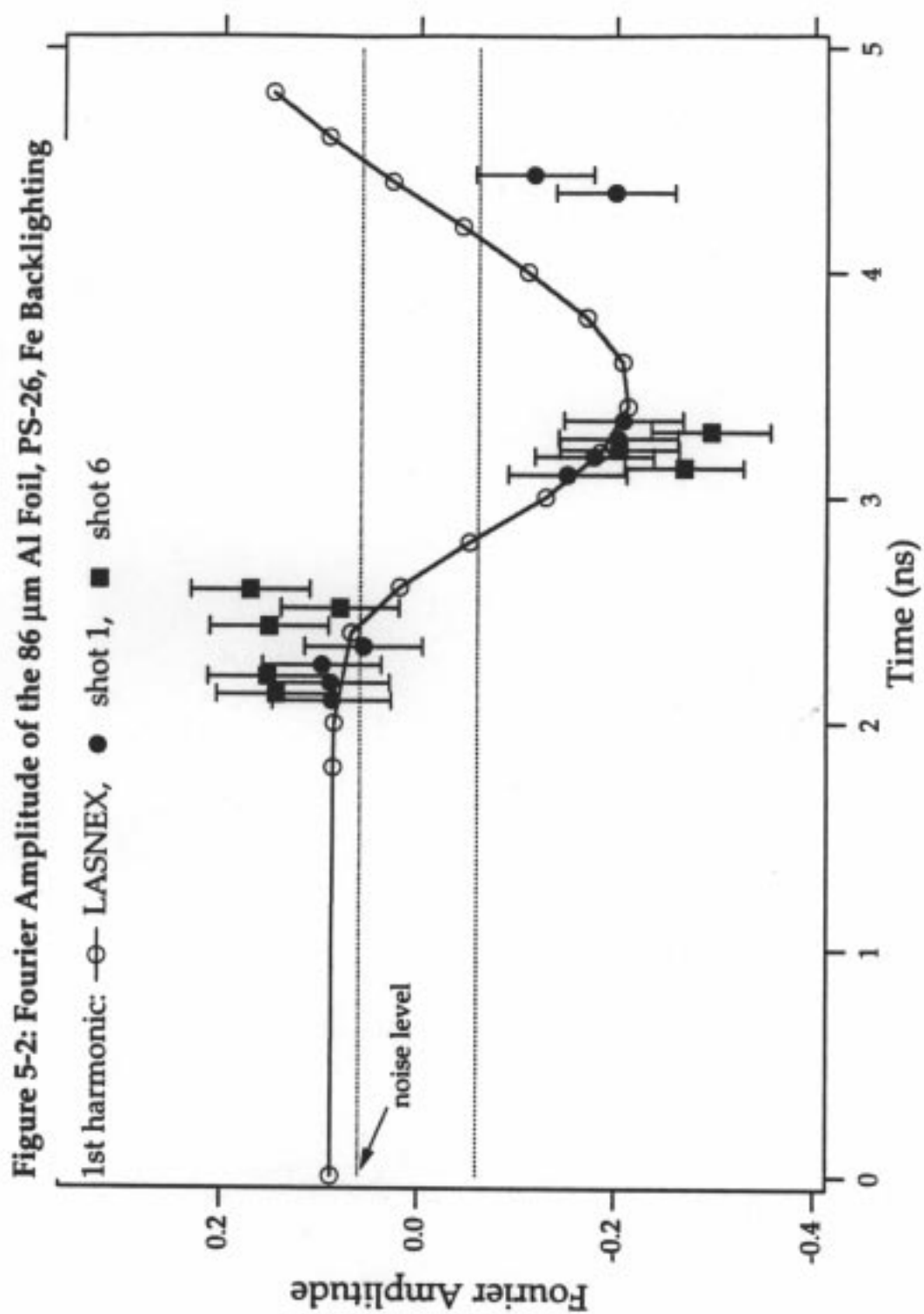
Interpretation of the data shown in the following figures must be made with care. Face-on data does not show the location of the perturbations, whether they are on the ablation surface, the cold surface, or are internal oscillations. Sometimes the results are a conglomeration of perturbations in all three locations. Modes that are in phase and of the same amplitude on both the ablation and cold surfaces are not observable, see Figure 5-1A. They produce a sinuous shape, which has an identical attenuation for X-rays passing through the trough or the peaks. The sinuous pattern occurs most frequently with modes that are coupling strongly across the interfaces and is thus more prevalent in the fundamental than in the harmonics due to the difference in wavelengths. In addition, the same perturbation with the same phase has a different Fourier transform phase depending

Figure 5-1: Fourier Amplitudes and Surface Perturbations



on whether it is on the hot or cold surface, see Figure 5-1B, because the phase of the attenuation curve changes.

The time history of the fundamental Fourier amplitude mode in the 86 μm , thick aluminum package is shown in Figure 5-2. The data is from shots 1 and 6 which used PS-26, the 2.2 ns pulse (see the appendix for shot details). The fundamental has a non-zero value at the beginning of the experiment, indicating that the diagnostic could see the initial perturbation. At about 2 ns, the shock arrived



at the cold surface and induced a Richtmyer-Meshkov instability. The perturbation phase-inverted and grew. Although the laser pulse ended at 2.2 ns, residual radiation from the hohlraum continued to accelerate the foil for perhaps another 600 ps. At 3.5 ns, the Fourier amplitude of the fundamental began to increase and phase-inverted a second time. Computational results indicate that this second phase-inversion was the result of the oscillation of a strong internal acoustic mode associated with the Richtmyer-Meshkov instability. The perturbation on the cold surface did not actually invert a second time.

The shock hit the cold surface about the time the pulse was turning off. As a result, the perturbation did not feed-out to the ablation surface in time for Rayleigh-Taylor growth. All of the activity observed in this foil is thus representative of the evolution of the seed for the Rayleigh-Taylor that feeds-out to the ablation surface. Only the fundamental is shown in Figure 5-2 because higher order harmonics did not appear in either the data or calculations. This would be consistent with only the Richtmyer-Meshkov instability, which produces harmonics slower than the Rayleigh-Taylor instability. In addition, side-on radiography showed growth of the cold surface perturbation, but a perfectly smooth ablation surface out to 4.5 ns, see Figure 5-3, indicating there was no Rayleigh-Taylor growth. The side-on data also supports the supposition that there was very little coupling between the cold and hot surfaces due to the excessive thickness of the foil. Feed-out is probably more difficult in thicker foils. Figure 5-3 shows two strips from the framing camera for both the thick and thin foils, with four images

Figure 5-3: Side-on Data of the 35 μm Al and 86 μm Al Foils

35 μm , shot 9

1.8 ns

1.86 ns

1.92 ns

1.98 ns



35 μm , shot 9

2.55 ns

2.61 ns

2.67 ns

2.73 ns



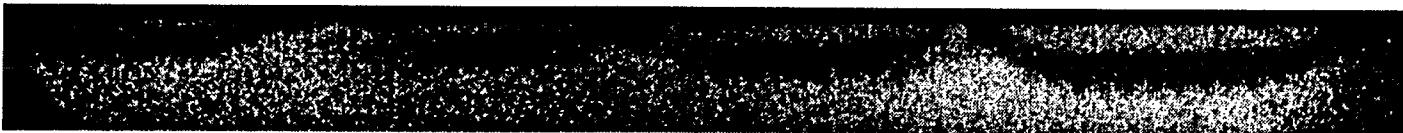
86 μm , shot 10

3.5 ns

3.56 ns

3.62 ns

3.68 ns



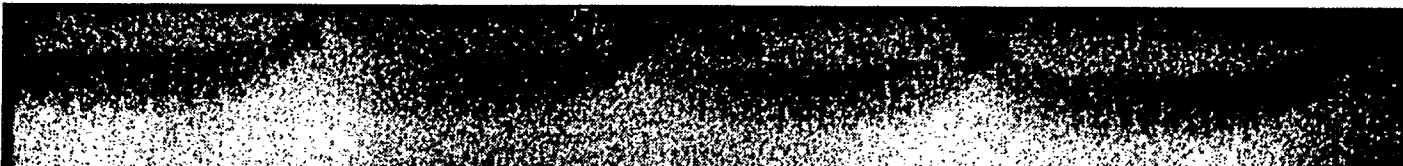
86 μm , shot 10

4.3 ns

4.36 ns

4.42 ns

4.48 ns



per strip. The thin dark area in the center of each image is the foil. Radiation comes from the dark area just above the foil, where the hohlraum is located.

Figure 5-4 shows the Fourier amplitudes from shot 3, the 35 μm , thin aluminum package driven with PS-26. Because of the relative thinness of this foil in comparison to the wavelength, there was a very strong coupling between the hot and cold surfaces. The shock hit the cold surface perturbation around 1 ns, and the perturbation began to phase-invert, producing a drop in the fundamental's amplitude. Before shock arrival, preheat created a small density gradient into the cold side vacuum, which may have partially stabilized the Richtmyer-Meshkov instability. By 1.4 ns a small perturbation appeared on the hot side of the package from feed-out and the package evolved rapidly into a sinuous shape. The sinuous pattern from feed-out may be easily observed in either the side-on data in Figure 5-3, or in the computational results in Figure 5-5. This was the first experimental confirmation of feed-out in radiatively driven foils. The sinuous shape reveals that the feed-out perturbation is in phase with the cold surface perturbation. This would be expected from instabilities strongly coupling across two interfaces.

The maximum density of the package dropped below the solid density of aluminum at 2 ns, and the package began to burn through. About this time the Rayleigh-Taylor instability caused a large growth in the ablation surface perturbation and spawned second and third harmonics. The Fourier phase of the second harmonic was opposite that of the fundamental and the third harmonic. The Ray

Figure 5-4: Fourier Amplitudes of the 35 μm Al Foil, PS-26, Ti Backlighting

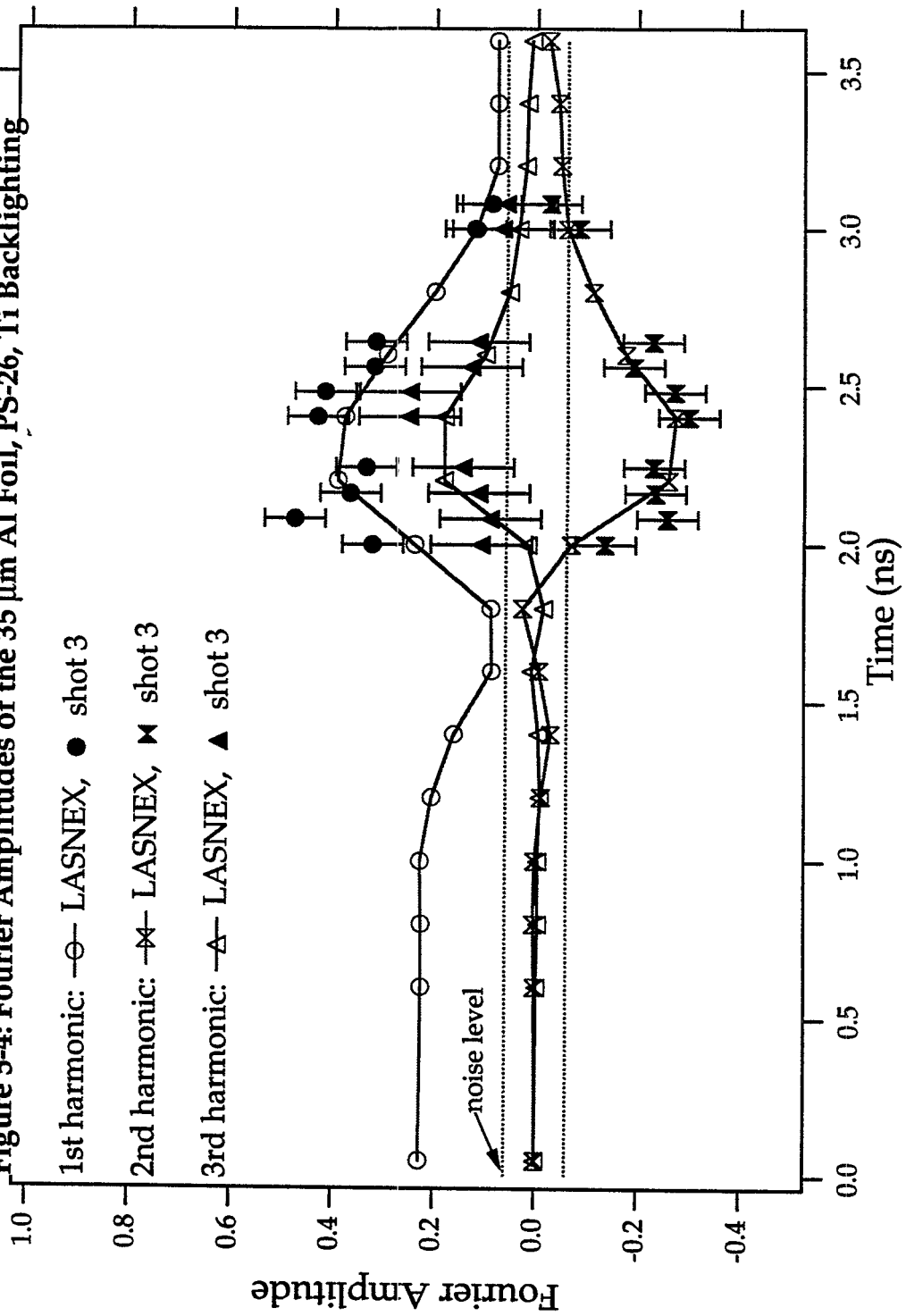
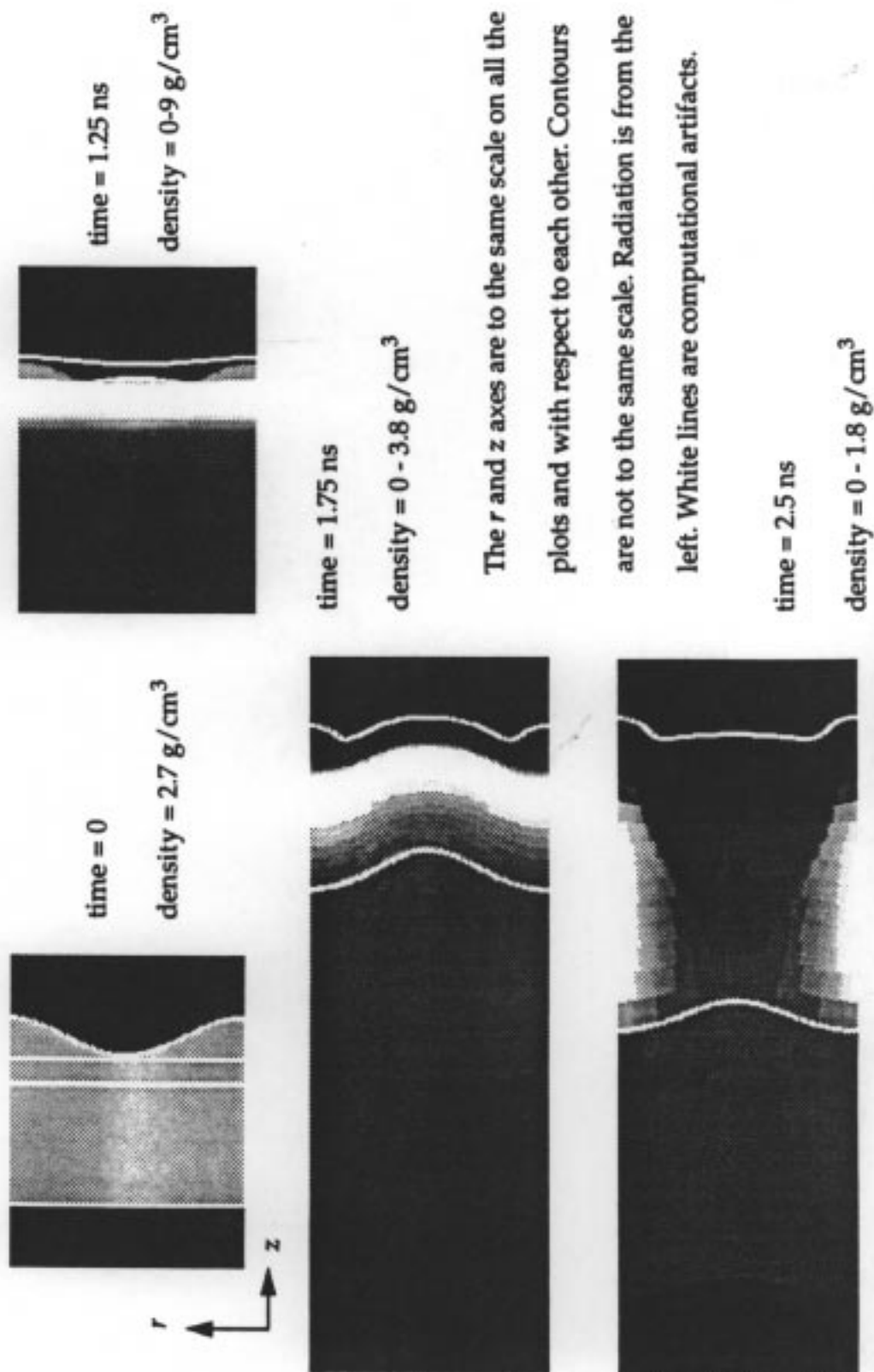


Figure 5-5: Density Contours of the 35 μm Al Foil, PS-26

leigh-Taylor instability reversed the phase inversion of the fundamental and by 2 ns the fundamental's amplitude increased above the original amplitude. After 2.5 ns, the package density continued to decrease as the foil broke apart, and the Fourier amplitudes decrease correspondingly. During late times, the foil evolved into a non-linear bubble and spike configuration as shown in Figures 5-3 and 5-5. The bubbles have burned through in both figures.

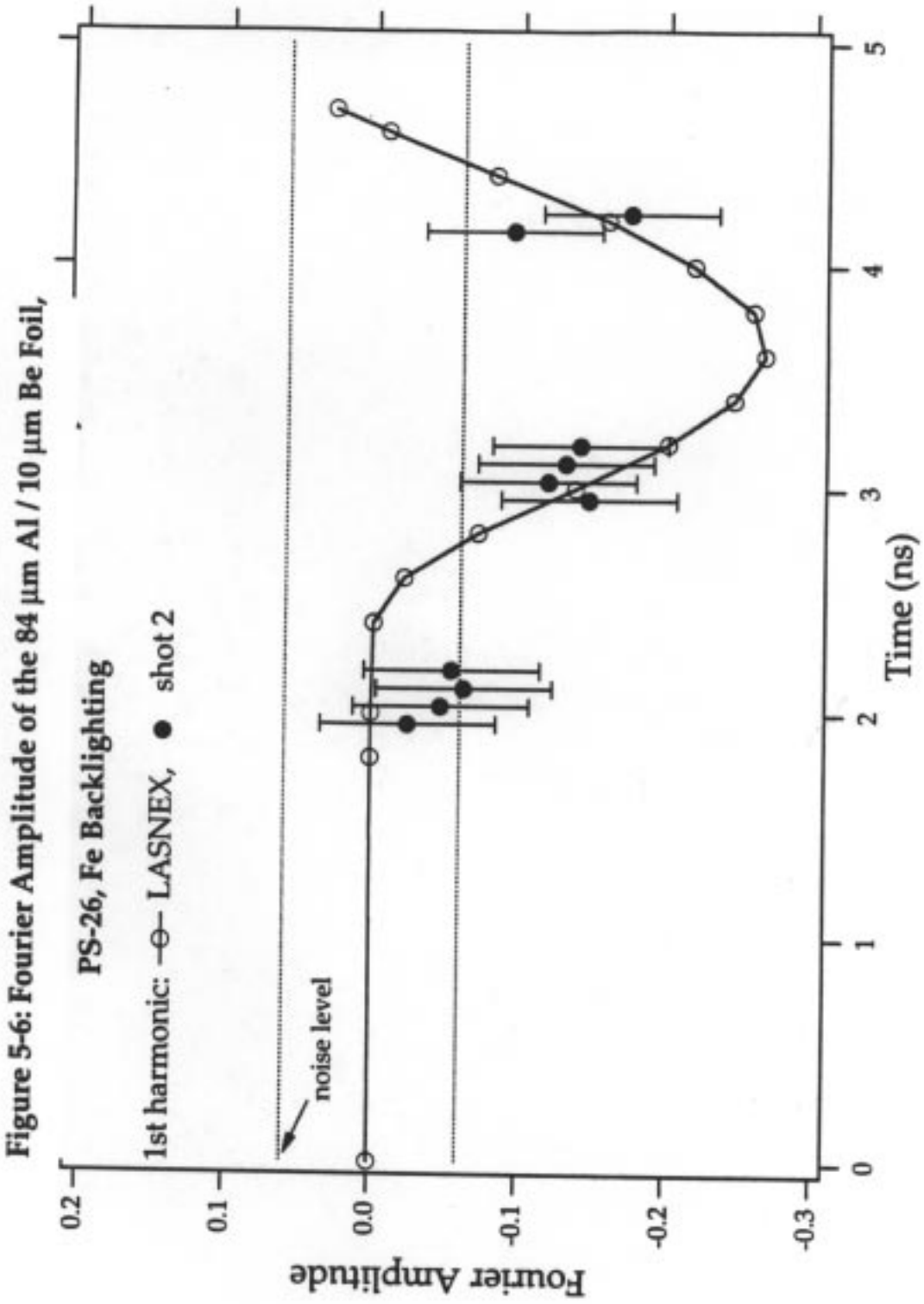
From the computational results, face- and side-on data, it is clear that the thin foil's physics is fundamentally different from the thick foil due to the greater interface coupling and the drive pulse being on during feed-out. This difference underscores the importance of thickness and pulse length in the feed-out process.

Beryllium was placed on the cold surface of some of the foils in order to observe any density jump effect, but also to observe feed-out of the seed. The beryllium was transparent to the backlighter, so when the seed moved from the beryllium into the aluminum, it could be observed. If the amplitude of the seed was smaller at the aluminum/beryllium interface than at the cold surface of the pure aluminum foils, this would help confirm that feed-out was dependent on thickness. The question of whether or not the feed-out seed decayed with distance from the cold surface was particularly interesting in light of the theoretical work discussed in chapter 2 predicting that the perturbation amplitude on a rarefaction wave was stable.

Face-on data from the thick aluminum/beryllium composite foil, shot

2, is shown in Figure 5-6. Notice that the diagnostic cannot see the initial perturbation, which is in beryllium. All of the observed perturbation growth is internal to the foil and has feed-out from the beryllium to the aluminum. A comparison between Figures 5-2 and 5-6 shows little difference. The beryllium was only 10 μm thick. If there was attenuation of the seed with distance from the cold surface, 10 μm might not have been large enough to observe the attenuation, so the result seems inconclusive.

A subtle aspect of the physics of the thick aluminum/beryllium foil was that the aluminum/beryllium interface could have become Rayleigh-Taylor unstable. This was an important concern in interpreting the data. If the interface was unstable, then perhaps the growth that was observed was due to the Rayleigh-Taylor instability and not due to the seed from feed-out. As long as the drive was on, the aluminum was pushing the beryllium and the interface was stable, but after the drive was off the foil began to expand. If the pressure dropped faster in the aluminum than the beryllium during the expansion phase, then a pressure gradient could form across the interface of the two fluids with an opposite slope to the density gradient. Density and pressure profiles with opposing slopes across the aluminum/beryllium interface would render the interface Rayleigh-Taylor unstable. The calculations indicated that this situation did not occur and that Figure 5-6 should only show feed-out into the aluminum.



Figures 5-7 and 5-8 show the Fourier modes for the 32 μm aluminum/10 μm beryllium packages shot with PS-26. The former plot is for shot 4 with a titanium backlighter, while the later plot shows shots 18 and 19 with a scandium backlighter. There was no concern in these shots of an unstable aluminum/beryllium interface as the drive was on almost the whole time of interest.

Two prominent peaks in the fundamental mode are seen at 1.6 ns and 2.4 ns. The second peak is probably Rayleigh-Taylor growth on the ablation surface. Its timing corresponds to Rayleigh-Taylor growth of the fundamental shown in Figure 5-4. The first, smaller peak is a mystery. Originally, the first peak was believed to be the feed-out seed entering the aluminum, but the peak is the wrong phase. In all the other experiments, both pure aluminum and composite, the initial growth and feed-out produces a negative Fourier amplitude phase. One would have expected a dip in the fundamental Fourier amplitude followed by a sharp rise from the Rayleigh-Taylor growth.

Another surprising and potentially important lesson was learned from the thin composite foils. The data did not reveal the presence of harmonics above the noise level in these packages. Calculations only predicted a second harmonic amplitude slightly above the noise level. One might therefore suspect that the second and third harmonics observed in the 35 μm pure aluminum packages were growing on the cold surface, but not on the hot surface. The lack of harmonics in the thick packages indicates that the Richtmyer-Meshkov instability was not producing the harmonics. Perhaps the higher harmonics observed in the 35 μm

Figure 5-7: Fourier Amplitudes of the 32 μm Al / 10 μm Be Foil,

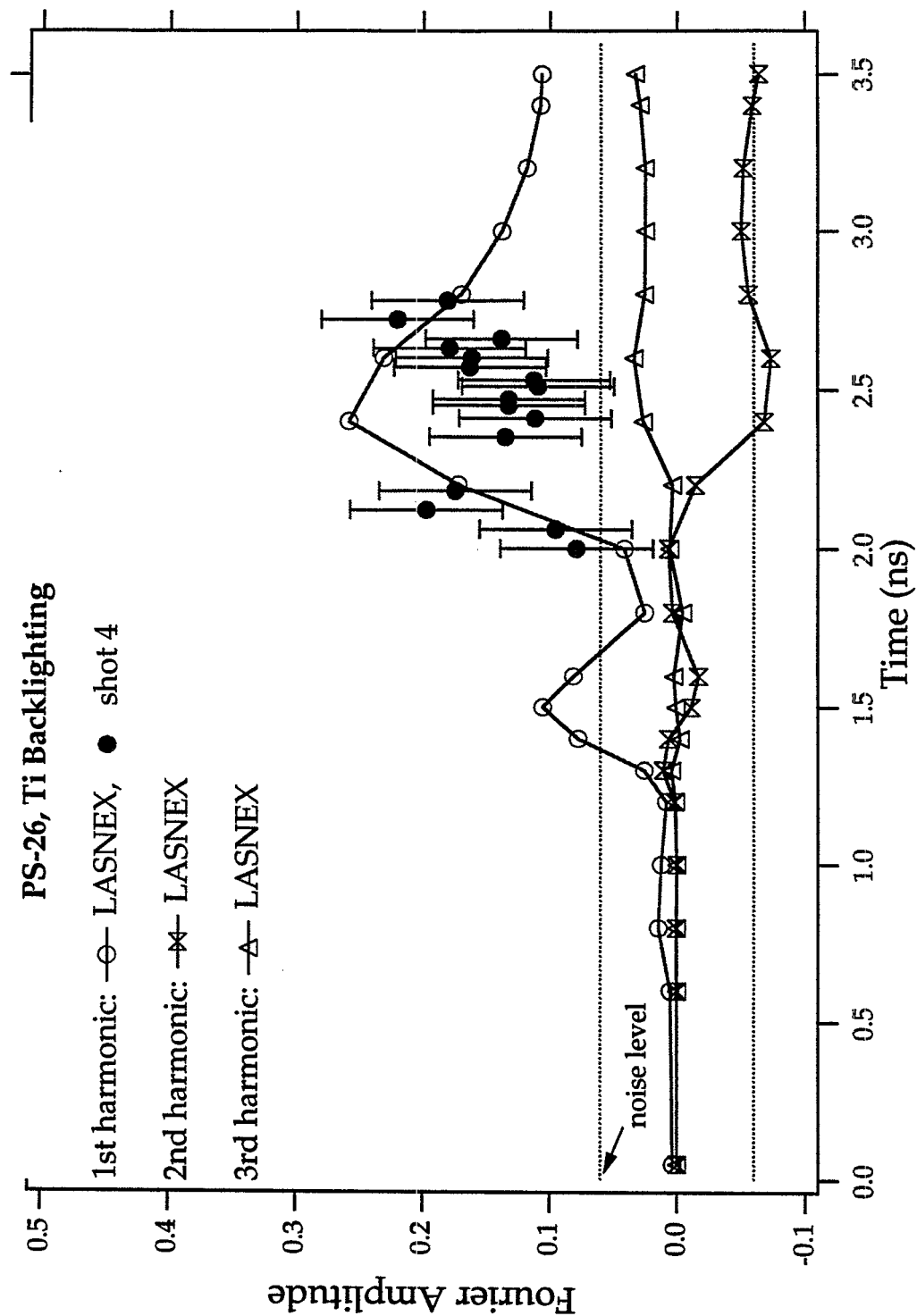
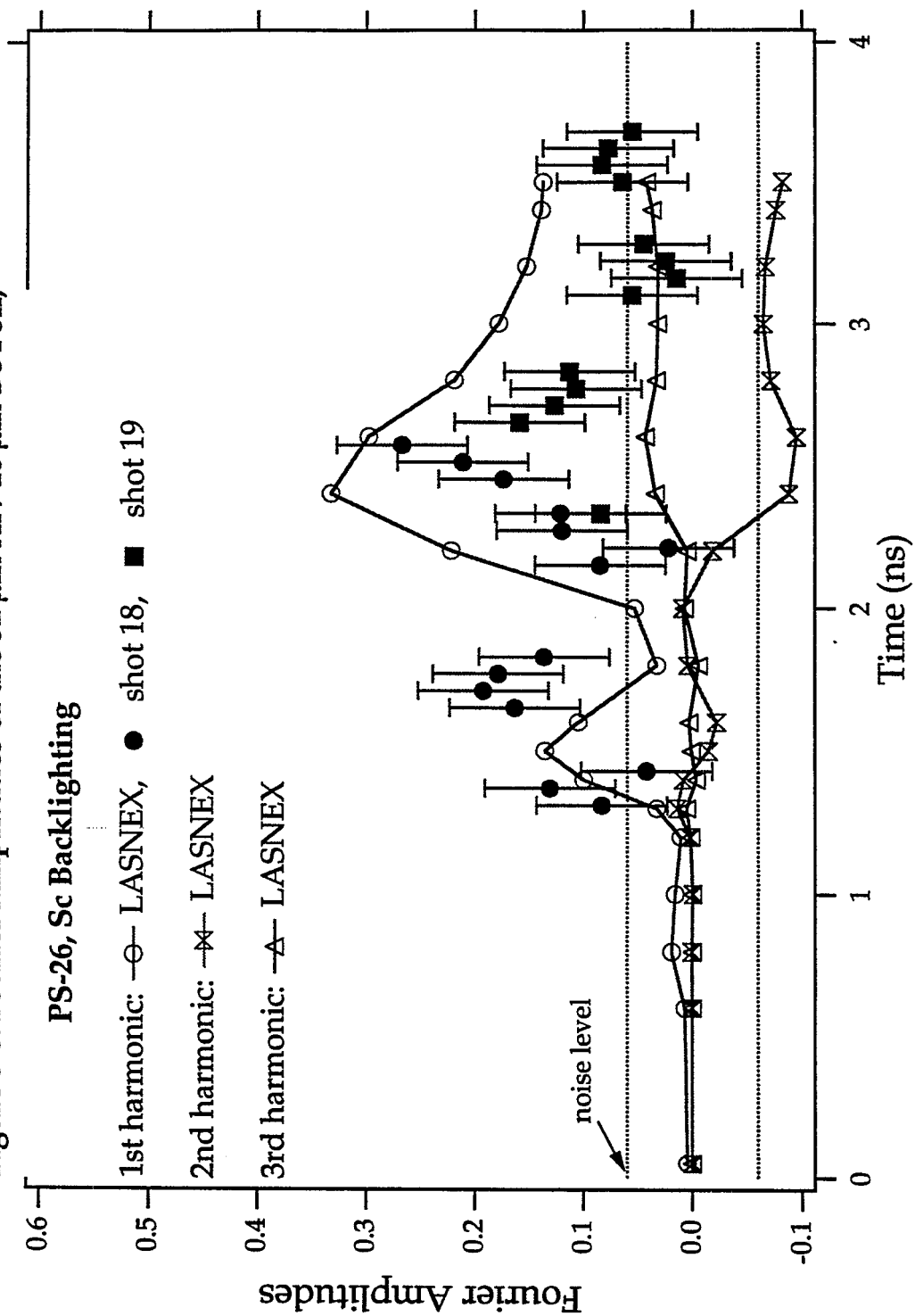


Figure 5-8: Fourier Amplitudes of the 32 μm Al / 10 μm Be Foil,



aluminum foil were both from Rayleigh-Taylor instability and on the cold surface. Linear coupling theory predicts that as a foil becomes much thinner than the perturbation wavelength, an instability on one surface will induce identical perturbation growth on all surfaces. The hot surface of the thin foils was ablatively stabilized, while the cold surface was not. The same instability may have acted as an ablative Rayleigh-Taylor instability on the hot side and as a classical Rayleigh-Taylor instability on the cold side after the instability had strongly coupled across the interfaces.

The dual ablative/classical nature of the Rayleigh-Taylor instability in these experiments is highly speculative but has important implications if it is true. As the ablator on an ICF capsule becomes thinner toward the end of the pulse, modes on the ablation surface created by the Rayleigh-Taylor instability feed-into the interior, degrading the yield. The ablative stabilization prevents the growth of high-order modes on the ablation surface. One might assume then that only low order modes would feed-into the interior from the Rayleigh-Taylor instability. The data presented here suggests that if the shell is thin and the Rayleigh-Taylor instability couples strongly to the interior surface, high order modes could be found growing in the interior as well as low order. Again, this is only speculation but seems worth investigating in future shots.

Intermediate to the strongly and weakly coupled cases is a foil that moved from weak coupling to strong coupling during the experiment. This is the most interesting case because it most closely resembles the realistic ICF situation.

Figure 5-9 shows the Fourier amplitudes for the 50 μm foils shot with PS-35, which was experiment 15. The intermediate coupling case is strongly dominated by the Rayleigh-Taylor instability and feed-in of the perturbation on the ablation surface back to the cold surface. The initial perturbation was placed on the cold surface, as in the other foils, but growth from the Richtmyer-Meshkov instability was very small compared to growth from the Rayleigh-Taylor instability after feed-out had occurred. One can clearly see Rayleigh-Taylor dominance in the data. There is a slight dip in the fundamental's Fourier amplitude until 3.5 ns from the Richtmyer-Meshkov growth and the feed-out moving toward the ablation surface. After 3.5 ns, there is a large positive-phase growth of the fundamental and harmonics appear. This later growth is from the Rayleigh-Taylor instability. Acoustic waves are also present as they were in the thick packages, but are not clearly discernible in the data.

The thickness of the intermediate foil is optimal for Rayleigh-Taylor growth. The foil is not so thick that there is no feed-out, but not so thin that it quickly burns through without giving the Rayleigh-Taylor a chance to grow. The 50 μm foil did not fall below the initial density of aluminum until around 7 ns, well after the hohlraum radiation from the 4.5 ns pulse had turned off. One could argue that the larger growth is simply due to the longer pulse and not the thickness, the thick foil did not exhibit any feed-out seed on the ablation surface in side-on radiography even at 4.5 ns. If the thick foil had been driven by PS-35, there might have been some Rayleigh-Taylor growth, but probably not as much as

Figure 5-9: Fourier Amplitudes of the 50 μm Al Foil, V Backlighting

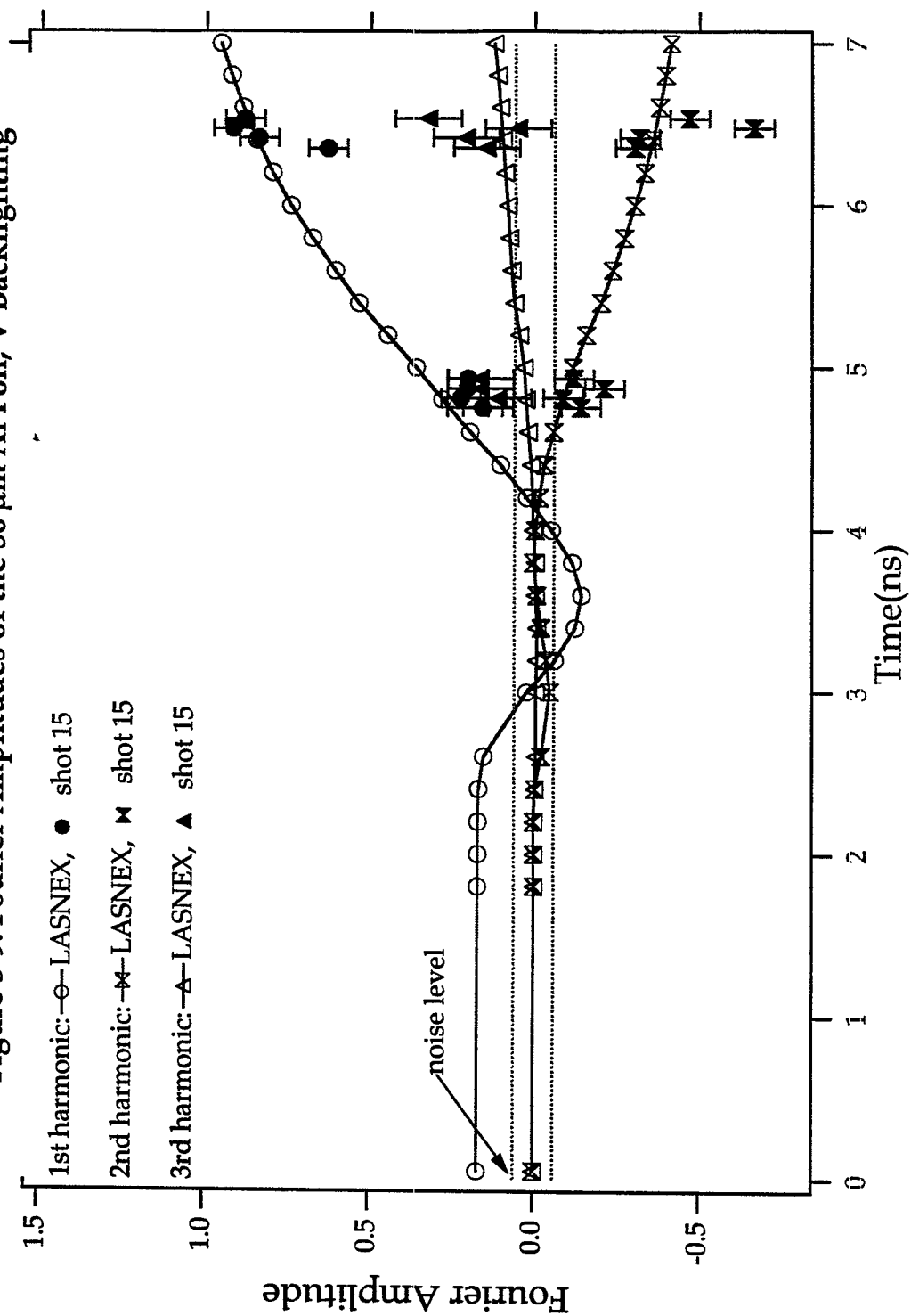
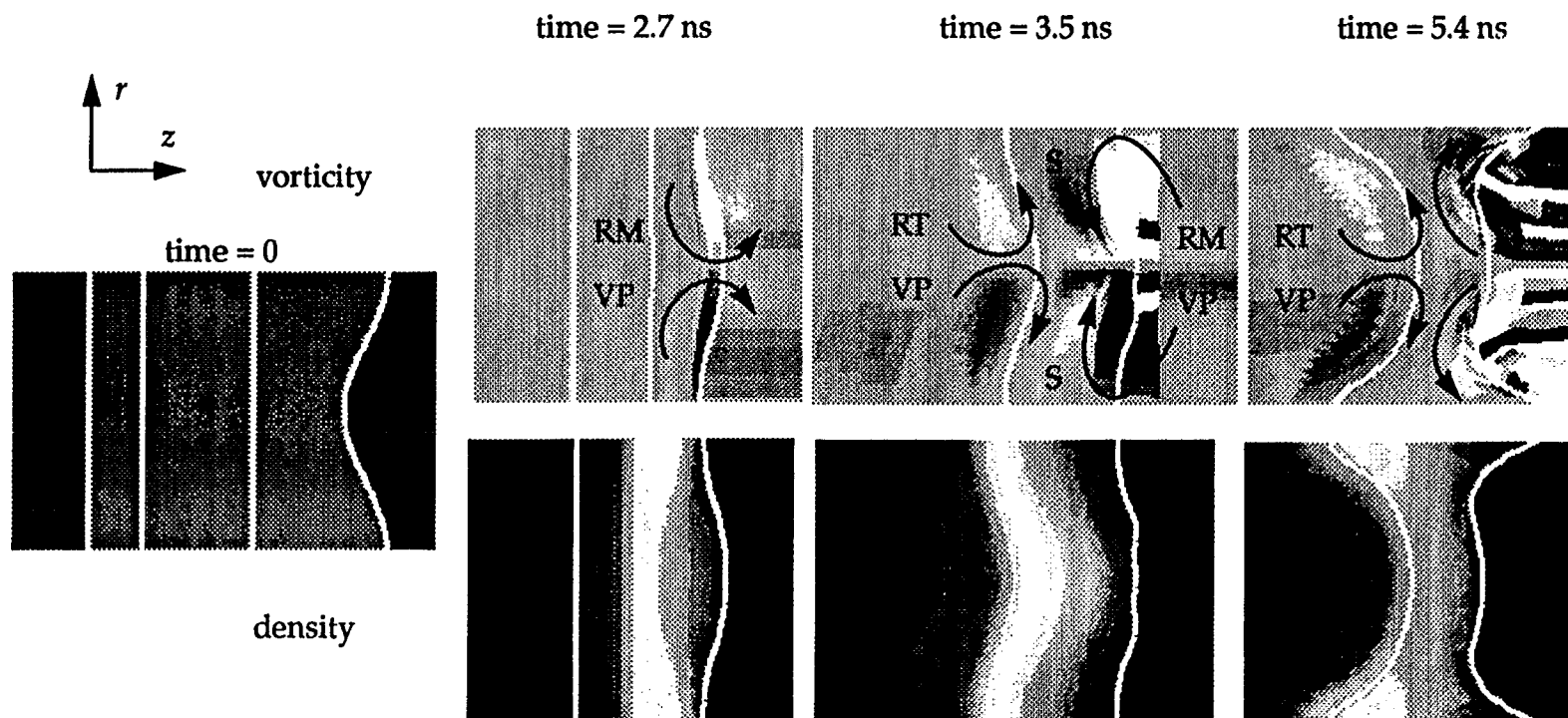


Figure 5-10: Density and Vorticity Contours of the 50 μm Al Foil, PS-35

The r and z axes are to the same scale on all the plots and with respect to each other. Contours are not to the same scale. White lines are computational artifacts. Radiation is from the left. RT VP and RM VP refer to the Rayleigh-Taylor and Richtmyer-Meshkov vortex pairs respectively. S symbolizes a shear vortex.



in the 50 μm foil. The importance of thickness to feed-out and feed-in is demonstrated by the 50 μm data.

Baltrusaitis' work revealed a very interesting fact about the Richtmyer-Meshkov instability [Baltrusaitis]. If there were two instabilities with opposing vortex pairs, each one on an interface of a thin ribbon of fluid, one instability would always dominate. When the thickness of the fluid layer was small enough for the instabilities to strongly couple across the interfaces, the fluid could no longer support both instabilities. The vortex pair of the stronger of the two would remain but also be weakened. A natural question for the 50 μm foil then, was how did the Rayleigh-Taylor and Richtmyer-Meshkov vortices interact as the foil narrowed, and which one dominated?

Figure 5-10 shows density and vorticity contour plots of the 50 μm foil. Each density plot was made at the same time as the vorticity plot beneath it. The first plot on the left shows the initial package configuration, with the radiation source coming from the left.

By 2.67 ns, the shock passed through the foil and a rarefaction wave may be seen moving back to the ablation surface. The perturbation carried by this wave is clearly evident in the density plot at this time. A Richtmyer-Meshkov instability took up residence on the cold surface, where its vortex pair may be seen in the vorticity plot. At 3.5 ns, the perturbation reached the ablation surface and the entire foil was imprinted, creating a sinuous shape. The vortex pair of a Rayleigh-Taylor instability may be found at this time on the ablation surface in

addition to the Richtmyer-Meshkov vortex pair on the cold surface. The vortex pairs of each instability rotated in the same direction, increasing the amplitude of the sinuous shape. The fluid velocity in the center of the foil from each instability moved in opposite directions and generated a shear vortex pair in-between the Richtmyer-Meshkov and Rayleigh-Taylor vortex pairs. Because the foil was still relatively thick, the shear was not excessive, and the two instabilities acted relatively independently.

Significant shear began to appear by 4.2 ns, and by 5.4 ns the Rayleigh-Taylor instability had coupled to the cold surface and overtaken the Richtmyer-Meshkov instability. The vortex pair on the cold side then had a rotation complementary to the Rayleigh-Taylor vortex on the ablation surface. Both of these vortex pairs pulled fluid from the center of the figure to the edges, moving the package from a sinuous to a bubble and spike shape. The bubble is in the center of the figure, with spikes at the edges. The presence of the Richtmyer-Meshkov instability thus seemed to delay the transformation of the package into bubbles and spikes by moving fluid in an opposite direction to the Rayleigh-Taylor instability. These results are very similar to those of the Baltrusaitis paper. An interesting question is if instabilities on the two interfaces had complementary instead of opposing vortex pairs, would the nonlinear evolution of the foil be enhanced?

Evolution from the sinuous to bubble and spike shape was experimentally observed in the thin packages with side-on radiography, see Figure 5-3. From 1.8 to 1.98 ns, the foil had an increasingly sinuous shape, with perturbations

on each side. From 2.55 to 2.73 ns, there was a distinct bubble and spike configuration. The spikes are the dark strips, the bubbles are the lighter spaces in between them. Although the Rayleigh-Taylor instability did not have the time to produce large growth in the thin foils, the evolution appears to be very similar to the 50 μm foil.

In addition to how feed-out varied with package thickness, the question of how a density jump affected it was both computationally and experimentally studied. Because the beryllium in the composite foils was a lower density than the aluminum and perturbation amplitude was the same in each, feed-out from differential acceleration was expected to be lower in the composite packages than in the pure aluminum packages. The density jump itself was not expected to directly affect the feed-out from differential acceleration, but was expected to lower the feed-out from interface coupling. The important question was then, how does a density jump affect the interface coupling?

To properly interpret the experimental data, one needed to ascertain whether differential acceleration or interface coupling was the dominant feed-out mechanism. This was accomplished by running calculations to estimate the individual amount of feed-out from each mechanism. The calculations involving differential acceleration are discussed first.

The thickness of each feed-out package was slightly larger if measured through the peak of the perturbation, and slightly smaller if measured through the trough. Two one-dimensional calculations were made of each of the four pack-

ages with feed-out, one with the larger thickness and one with the smaller thickness. Both one-dimensional foils started at the same position. The location of the ablation fronts was defined at $\max \left| \frac{1}{\rho} \frac{\partial \rho}{\partial z} \right|$. Half the difference between the two ablation front positions was defined as the amplitude of the hot surface perturbation from differential acceleration. This manner of calculating feed-out from differential acceleration has a difficulty. In a two-dimensional foil, the Richtmyer-Meshkov instability and acoustic waves move material from the peak of the perturbation to the troughs, saturating differential acceleration after about a nanosecond. These calculations thus provide an upper limit on the feed-out.

To calculate feed-out from interface coupling, a set of two-dimensional calculations were run using a pressure source to generate the shock instead of radiation. Acceleration effects were minimized in this fashion. Because the calculations were Lagrangian, perturbation amplitudes were easily obtained by subtracting the position of the top and bottom of each interface and dividing by two. Thinner foils were used in the pressure source calculations than in calculations with radiation. For the pure aluminum packages, 20 μm was used in place of 35 μm , and 35 μm was used in place of 50 μm . For the foil with beryllium, 10 μm of beryllium was used in both cases, and 12 μm of aluminum replaced 32 μm . Interface coupling is strongly dependent on thickness. By the time the shock had reached the back surface of the packages, compression and ablation had significantly reduced foil thickness. Foil thicknesses at the time of shock arrival at the

cold surface were estimated using the calculations with radiation. There are some problems with adjusting the thickness in an attempt to more accurately model the interface coupling. It is not entirely clear that matching thickness is more important than matching the total mass of the foil when simulating interface coupling with compressible fluids, but one cannot do both. Also the thickness of the radiatively driven foil is a function of time, which could not be simulated in the pressure source calculations.

The pressure sources were adjusted to create shocks with the same Mach number and density jumps as radiation. Calculations simulating the PS-35 shock worked well, but when the pressure was increased to simulate the PS-26 shock, numerical instabilities killed the calculation. The mesh was perfectly smooth with no perturbations of any kind, and it would still tangle around the shock before it reached the foil.

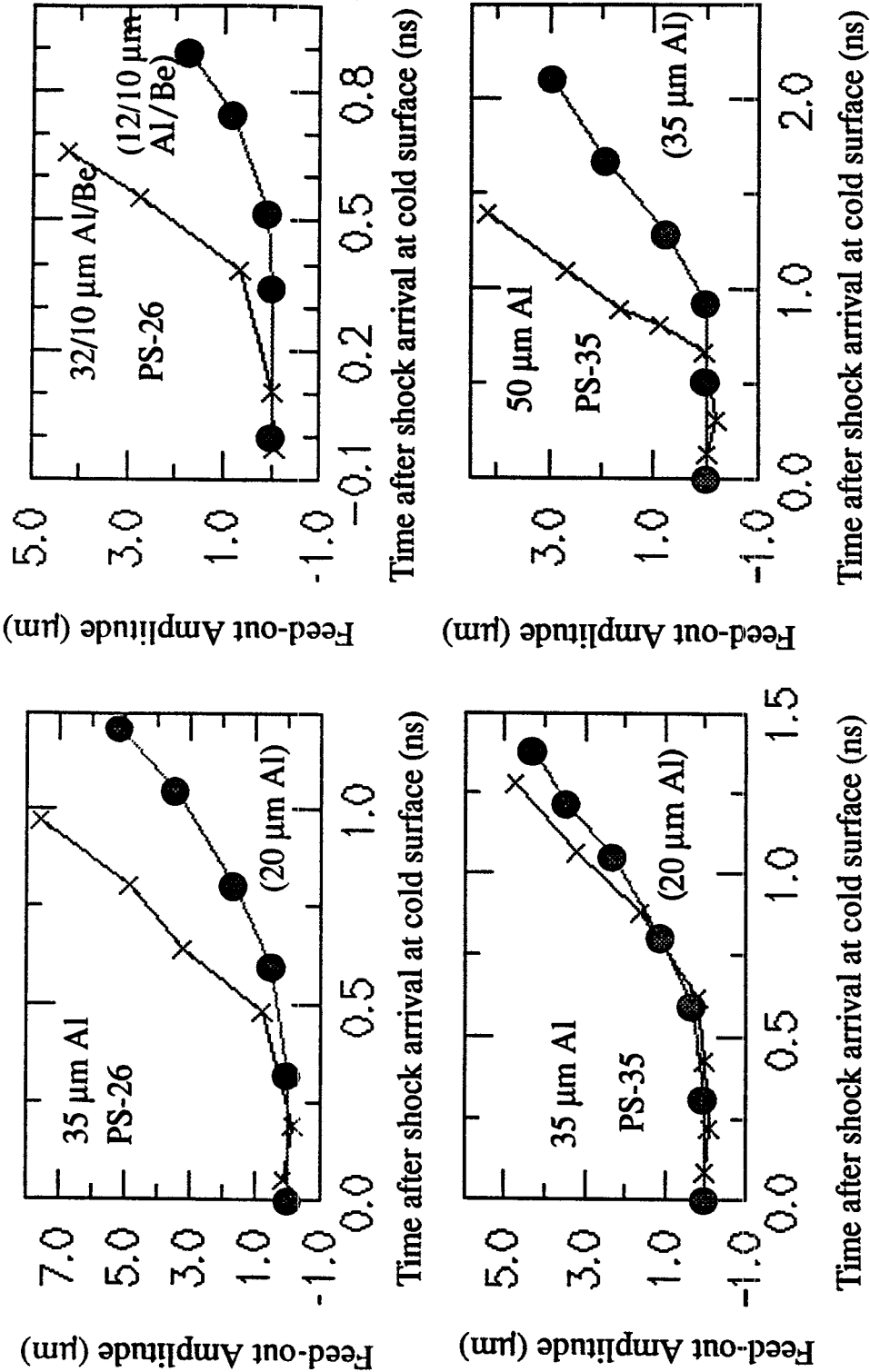
In order to avoid the mesh tangling problem, two calculations were used to simulate the PS-26 packages. The first was a two-dimensional run with a shock strength corresponding to PS-35. The second was a one-dimensional run with a shock strength corresponding to PS-26, which did not have the numerical instabilities. Perturbation growth on the "hot" surface was measured in the two-dimensional case and multiplied by the ratio of postshock velocities of the one- to two-dimensional calculations. Use of the postshock velocity to estimate the growth from a stronger shock was based on the impulsive model and Mikaelian's theories.

The final results are thus not exact in either case, but they provided a way of estimating each effect. They are plotted in Figure 5-11. In all cases, the differential acceleration is larger than the interface coupling, but the reader must keep in mind that differential acceleration will saturate faster than Figure 5-11 shows. Both mechanisms were probably important in the feed-out experiments, but this conclusion should not be generalized. Foils with other sizes and pulses could have differential acceleration or interface coupling as insignificant mechanisms.

With the understanding that changes in differential acceleration probably obscured the density jump effect on interface coupling, consider the peak amplitudes of the fundamental in Figures 5-4 and 5-7 and 5-8. The composite packages appear to have a smaller fundamental growth from the Rayleigh-Taylor instability, but why? The smaller growth could be in part from a smaller feed-out from the differential acceleration. It could also be in part because the acceleration of the composite package is slightly less than that of the pure aluminum. The two packages were initially designed to be mass matched, but due to an error in fabrication, the composite package was slightly thicker and more massive than the pure aluminum. The higher mass of the composite package resulted in a lower acceleration and slower Rayleigh-Taylor growth than for the pure aluminum package, but it was not enough to account for the difference in peak amplitudes alone. A third factor is the perturbation on the aluminum/beryllium interface. The

Figure 5-11: Feed-out from Differential Acceleration and Interface Coupling (Computational Results)

X: Feed-out from differential acceleration. ●: Feed-out from interface coupling.



pressure source calculations described above implied that internal perturbations could be larger than the surface perturbations. Because the X-rays were interacting with perturbations on both surfaces, the amplitude of the fundamental was affected by this also. As a result, it is difficult to say exactly what effect the density jump had on the interface coupling feed-out in these experiments, other than it was not exceptionally large.

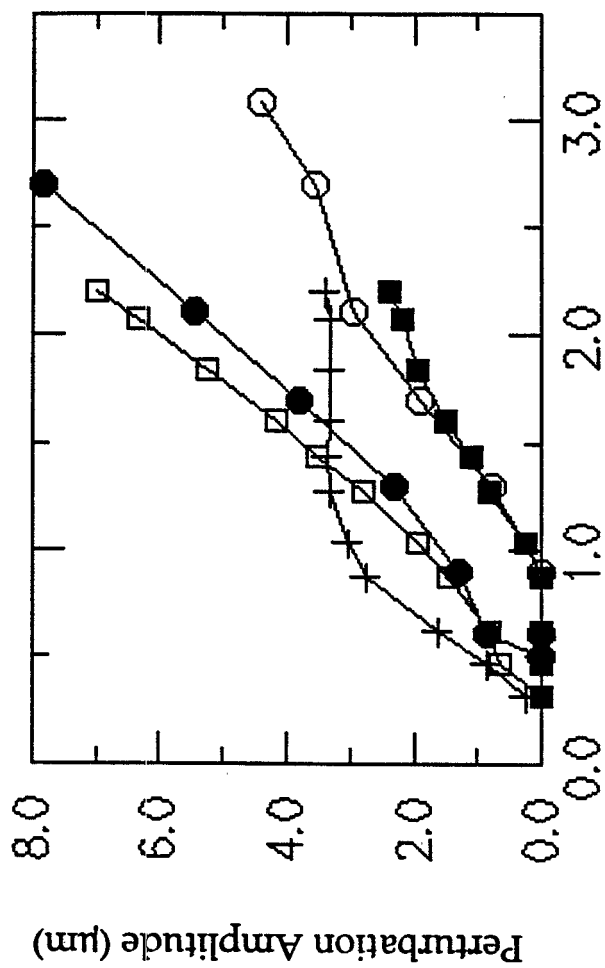
Because of the ambiguous nature of the data, additional calculations were made specifically to address the effect of a density jump on interface coupling. The calculations were two-dimensional pressure source calculations again. Two pressure source calculations were run with matched thicknesses, one with 35 μm of aluminum and the other with 25 μm aluminum on the front and 10 μm beryllium on the back. Again, a 4 μm amplitude, 50 μm wavelength perturbation was placed on the rear surfaces. A shock corresponding to the PS-35 drive pulse was sent through each.

Figure 5-12 shows the evolution of the five interfaces, including the aluminum/beryllium interface. The composite foil had slightly less feed-out than the pure aluminum, but not a lot. The density jump did not appear to affect the interface coupling significantly. Interestingly, the aluminum/beryllium interface had a larger perturbation than either the front or back surfaces until it reached saturation. The internal perturbation in the pure aluminum foil was likewise larger than the perturbations on either of its surfaces. The amplitude of the perturbation on the rarefaction wave could clearly be seen in each case and was almost the same.

Figure 5-12: Feed-out from Interface Coupling with a Density Jump (Computational Results)

25 μm Al / 10 μm Be: \square : "cold" surface, \blacksquare : "hot" surface, + : Al/Be interface

35 μm Al: \circ : "cold" surface, \bullet : "hot" surface



Time after shock arrival at the back surface (ns)

The implication of both the calculations and experiments was that a density jump did not have a large affect on the interface coupling feed-out.

Three final topics will now be discussed that may not relate to the feed-out process. The first is the strong acoustic mode observed in many of the foils. Next, an experimental discrepancy, a large second harmonic is reviewed. Finally, the only major discrepancy between the experiments and calculations will be discussed.

An internal oscillatory mode was computationally observed in every foil and experimentally evident in the thick foils. The mode was of interest for two reasons, it might affect the seeding of the Rayleigh-Taylor and could represent a third instability in the foils. The oscillations in the thick foils had to be acoustic waves instead of an atmospheric type mode because the foils were not accelerating while the waves were present. Waves in the other feed-out packages occurred during times of acceleration and were some type of atmospheric type mode, either an acoustic, gravity, or Lamb mode. Both the Lamb and gravity modes offered interesting possibilities in that they could become unstable and grow, although the most likely possibility was always the acoustic mode which commonly accompanied the Richtmyer-Meshkov instability. Unfortunately, the modes were very difficult to observe in the calculations because the foils usually burned through before the waves completed one cycle. In addition, fluid motion from the Richtmyer-Meshkov and Rayleigh-Taylor instabilities complicates their study.

To observe the waves more clearly, calculations were run with pure beryllium foils and PS-35. In beryllium, the wave could be observed over several periods while the package was still accelerating and could be seen continuing to oscillate well after the foils burned through. The foils were 50 μm thick with perturbation amplitudes of 0.5 μm . To increase the foil lifetime during the pulse and decrease shock strength to assure linearity, total laser energy was decreased to 15 kJ. Wavelengths from 5 to 50 μm were run. There was no guarantee that the waves in the beryllium calculations were the same as those of the feed-out foils, but the feed-out waves are unobservable over multiple wavelengths.

The term "turn around" will be used here to designate points where the first derivative of the fundamental Fourier amplitude changed sign, such as at 3.5 ns in Figure 5-2. The results seemed to confirm that these modes were stable, acoustic modes. The amplitude of the waves oscillated randomly with time around the amplitude at the first turn around and was a function of the wavelength, although this cannot be explained. There was no obvious growth of the amplitude over time, so the waves did not appear to be internal instabilities, such as a Lamb mode. The time between shock arrival at the cold surface and the first turn around was not indicative of a half period. A half period was more accurately estimated as the time between the first and second turn around.

The periods approximately matched those for an acoustic mode, but, after the calculations were completed, a possible error was discovered. Linear theory suggested that the physics of the beryllium packages may not have supported

the existence of gravity modes, unlike the feed-out foils.

An experimental discrepancy occurred in the 35 μm foils shot with PS-26 and there was not a sufficient number of shots to explore it thoroughly. A large second harmonic appeared in two of the three shots taken with this foil, which disagreed with previous shot data and computational predictions. Figure 5-13 shows the data for shots 8 and 17, which were identical to shot 3 in Figure 5-4, with the exception that a scandium backlighter was used at 4.3 keV instead of titanium at 4.7 keV. The difference in backlighter energies between shot 3 and shots 8 and 16 accounts for the slightly lower initial Fourier amplitudes of the packages, as the opacities were a little different. Figure 5-14 shows raw data from the framing camera for shots 3 and 8. The frequency doubling is clearly seen in one shot but not the other.

Two particularly unusual aspects of this large second harmonic were that it attained an amplitude much larger than the fundamental, and this large amplitude was early in time, just after the shock hit the cold surface. These two facts suggest this was not a non-linear mode coupling effect, such as described by Haan's theories. The second harmonic decreased rapidly in amplitude after about 1.8 ns, suggesting that the effect was short lived. Several possibilities were considered.

A machining error could have occurred in package fabrication, resulting in an initial second harmonic. A LASNEX calculation was run which included an initial second harmonic with the fundamental. The second harmonic's ampli-

Figure 5-13: Fourier Amplitudes of the 35 μm Al Foil, PS-26, Sc Backlighting

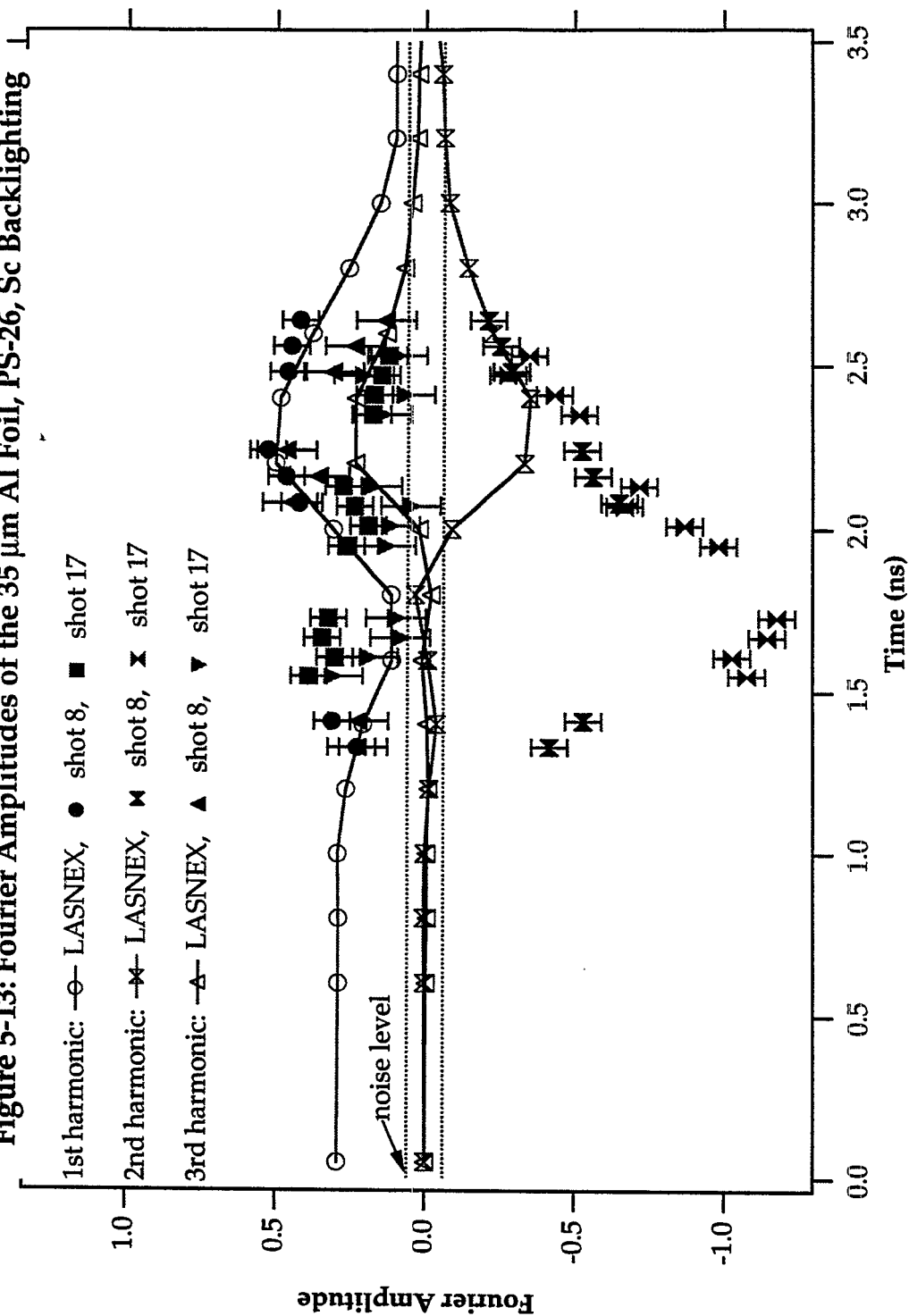
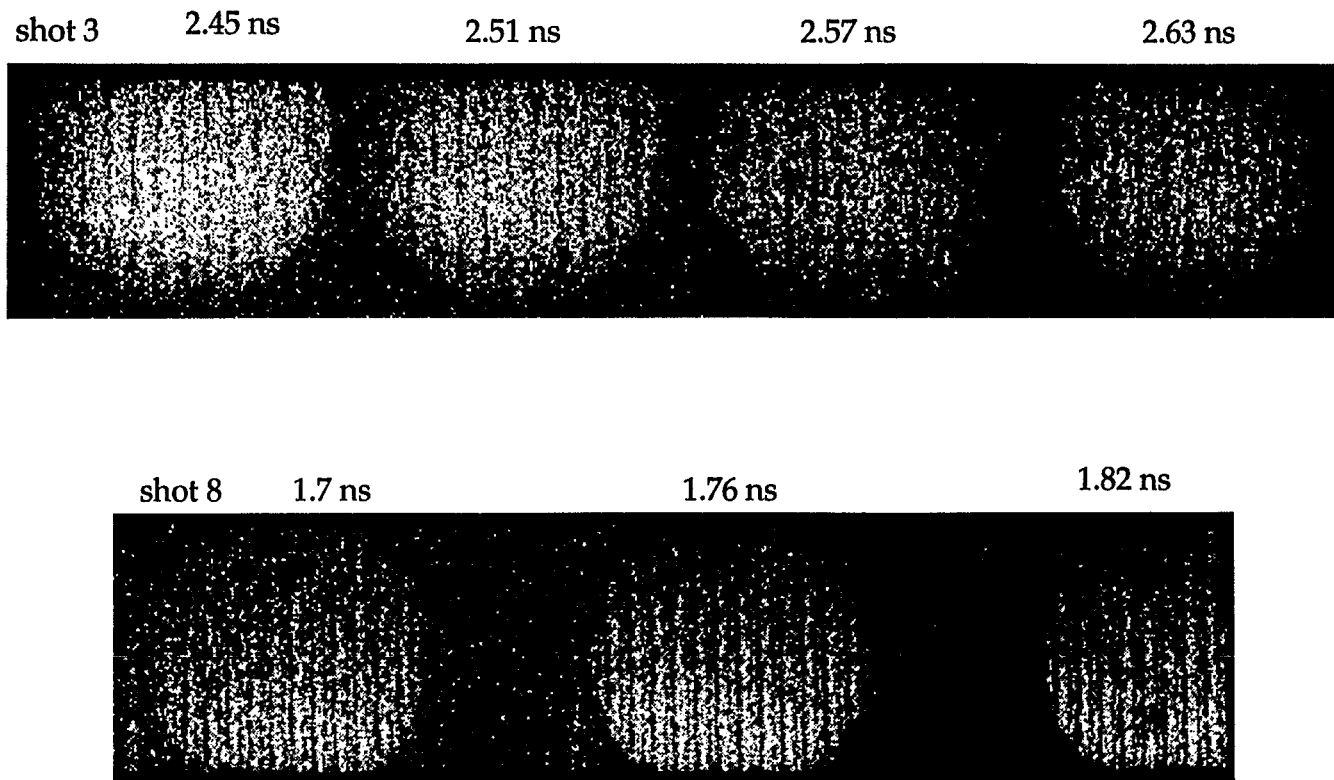


Figure 5-14: Face-on Data of the 35 μm Al Foil With and Without Frequency Doubling



tude was set to ten percent of the amplitude of the fundamental. Subsequent Fourier analysis showed no growth of the second, and even a slight decrease until about 1.8 ns. The final result was very similar to Figure 5-4. In addition, before the targets were fielded, the perturbations on some of the packages were scanned and recorded. Preliminary Fourier analysis of the available scans did not indicate an initial second harmonic present.

Excessive preheat from the gold M-band was considered a possibility because it would fit the early time nature of the phenomenon. The perturbation troughs would be preheated slightly more than the peaks. The preheat differential could result in a discharge of vaporized material by the troughs, which would form into jets of material. The jets and perturbation peaks could form a large second harmonic.

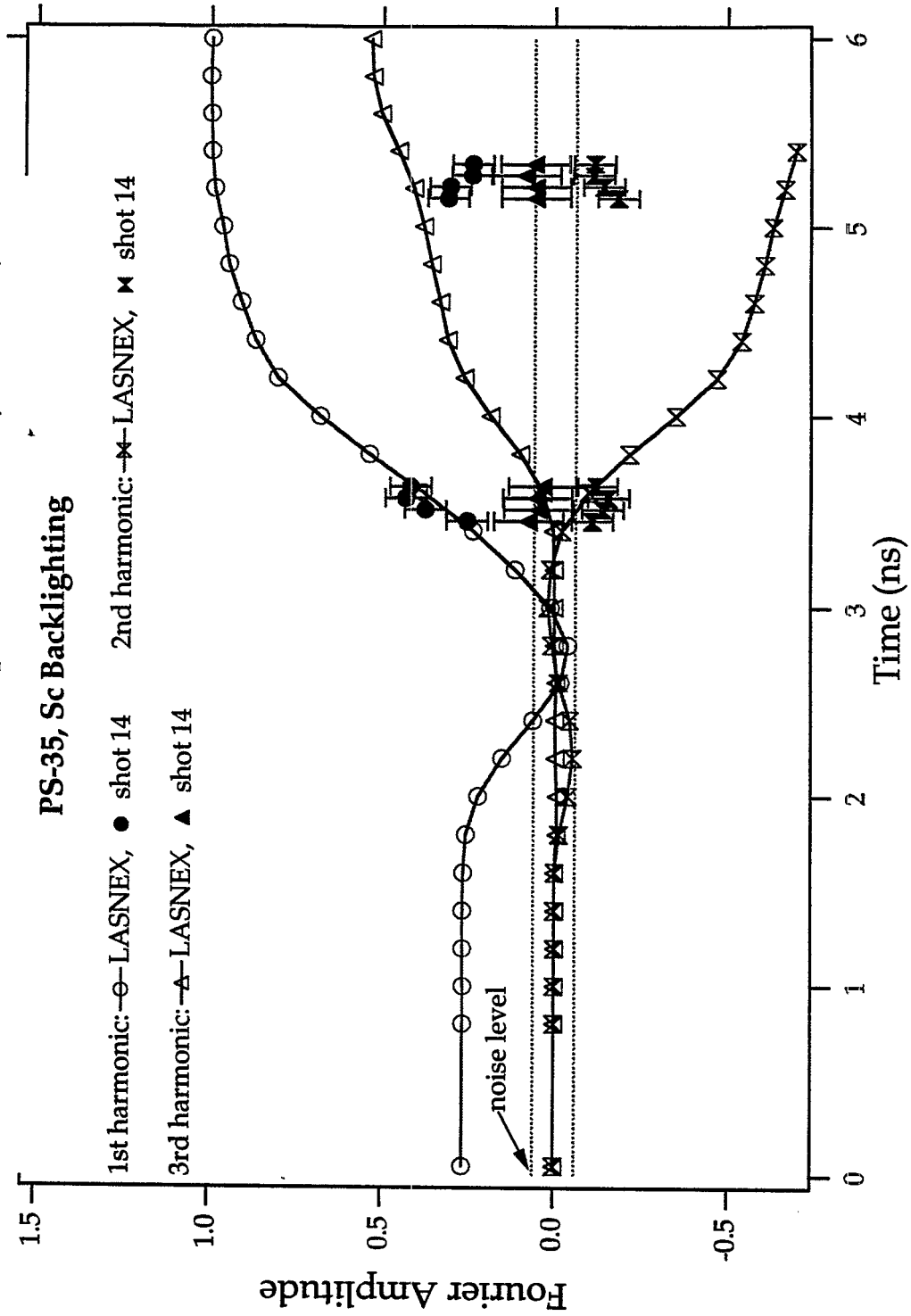
Another LASNEX calculation was run with the intensity of all radiation bins from 2.2 - 8.4 keV increased an by order of magnitude. Fourier analysis showed a time history similar to Figure 5-4, with the difference that the increase and decrease in the harmonic amplitudes was much steeper around 2.4 ns. Preheat did not appear to be the answer.

A third possibility was entertained. Schappert and Hollowell found a large second harmonic in their experiments which was attributed to a high order mode coupling into the second [Hollowell]. However, the second harmonic in this case appeared late in time. RAGE was more capable of modeling this effect than LASNEX, and Hollowell ran a RAGE calculation simulating the 35 μm aluminum

package. The perturbation was modeled by square zones approximately $0.6\text{ }\mu\text{m}$ in thickness in a stair step fashion, creating a high order mode similar to the machining process. No large second harmonic appeared, either as observed in the Schappert or feed-out shots. The source of the large second harmonic remains unknown.

A discrepancy was also found between the calculations and experiments in the case of the $35\text{ }\mu\text{m}$ foil shot with PS-35, see Figure 15. LASNEX predicted much larger modal amplitudes than observed during late times, after the package had burned through at 5 ns. The reason for this is unclear. It was suggested that this discrepancy could be accounted for by tilting of the spikes out of the direct line of sight of the camera. Side-on radiographs of the other feed-out packages do not show such a tilt in the spikes, although bowing is evident. Although the foil shows a large amount of bending as it lifts off from the hohlraum, the spikes appear to all be perpendicular to the hohlraum and the drive, both in the thin and thick foil cases. Hollowell and Schappert had a similar discrepancy between RAGE calculations and experiments [Schappert, Hollowell].

Figure 5-15: Fourier Amplitudes of the 35 μm Al Foil,



6. Conclusion

Feed-out is the communication of a perturbation from the cold surface of a radiatively driven foil to the ablation surface, and its subsequent growth. Differences in feed-out are believed to be partially responsible for the superior robustness of beryllium NIF capsules over plastic capsule designs in regard to interior perturbations. Feed-out is an important hydrodynamic effect in ICF because it couples the large internal perturbations with the long-duration, strong ablation surface instability.

In order to better understand the nature of feed-out, an experimental and computational campaign was undertaken to study the effects of a density jump and variations in coupling on the phenomena. Planar aluminum foils with a perturbation on the cold surface were driven with radiation from a hohlraum. Thickness and pulse length were adjusted to observe the following cases: weakly coupled hot and cold interfaces, strongly coupled interfaces, and an intermediate case which moved from independent Rayleigh-Taylor and Richtmyer-Meshkov instabilities to coupled instabilities as the package burned through. Composite packages of aluminum ablators and beryllium payloads were used to observe the effect of a density jump. The beryllium was transparent to the backlighter, so feed-out into the aluminum was visible. This was the first campaign known to the author undertaken specifically to investigate feed-out in a regime relevant to ICF.

The existence of the feed-out phenomena was confirmed experimentally for the first time in radiatively driven foils using side-on and face-on radiog-

raphy. The thickness and pulse length were found to be crucially important, as they determined the level of interface coupling. The thick foil showed weak coupling of the cold and hot interfaces, while the thin foil showed a strong and fast coupling. Because of the short pulse and package thickness, only the Richtmyer-Meshkov instability was present in the thick foil. Both Richtmyer-Meshkov and Rayleigh-Taylor instabilities were present in the thin foil. The cold surface perturbation was observed feeding-out into the aluminum ablator from the beryllium payload in the thick aluminum/beryllium composite package. In the thin composite case, a curious peak in the fundamental amplitude was observed during the time feed-out was expected. The peak was the opposite phase from what one would expect of feed-out. There was some evidence that the Rayleigh-Taylor instability in the thin foil acted as an ablative instability on the ablation surface and as a classical instability on the cold surface. If the Rayleigh-Taylor actually had a dual behavior, then the instability could generate higher harmonics in the interior of ICF capsules than on the exterior ablation surface.

The package with intermediate coupling showed a large amount of Rayleigh-Taylor growth. The physics of this package was dominated by the Rayleigh-Taylor growth feeding-back to the cold surface. Calculations showed the development of two relatively independent instabilities in the beginning, a Richtmyer-Meshkov on the cold surface and Rayleigh-Taylor on the ablation surface. During this time, the foil maintained a sinuous shape. As the package burned through and the perturbations grew, the vortex pair of the Rayleigh-Taylor

became dominant over the Richtmyer-Meshkov vortex pair, evolving the foil into a non-linear bubble and spike shape.

Calculations indicated that both differential acceleration and interface coupling were important to the feed-out process in the experiments presented here. Interface coupling feed-out is the seeding of the Rayleigh-Taylor instability by the Richtmyer-Meshkov instability coupling to the ablation surface. Differential acceleration feed-out is the seeding of the Rayleigh-Taylor instability by differences in the acceleration of the fluid columns running through the troughs and peaks of the cold surface perturbation. Experimental data and calculations indicated that, contrary to the original hypothesis, a density jump may not greatly affect feed-out from interface coupling. There is the possibility of a moderate to small effect. The density jump was not expected to affect feed-out from differential acceleration, however, the composite packages had a smaller mass differential between the peaks and troughs of the perturbation because beryllium is not as dense as aluminum. The lower mass differential should have resulted in less feed-out from differential acceleration.

Three interesting observations were made that do not necessarily relate to feed-out. Large oscillatory modes were computationally observed in all the foils and experimentally observed in the thick foils. These modes were believed to be an acoustic wave in the thick foils and an acoustic-type atmospheric mode in the other packages. Secondly, a large second harmonic was observed in two of the three thin foil shots with the 2.2 ns pulse. This large harmonic did not agree with

the first experimental data or the calculations. Lastly, there was a discrepancy between the computationally predicted growth during late times of the 35 μm foil shot with the 4.5 ns pulse and the data. The data showed much less growth than predicted. The reasons for the large second harmonic and low growth in the PS-35 foil are unknown. Possible reasons are discussed in chapter 5. A summary of the experiments and their results is shown in Table 5-1 below.

Table 5-1:

Package Thickness (mm), Pulse Length (ns)	Results
86 Al, 2.2	Weak interface coupling. Richtmyer-Meshkov instability only. Strong acoustic waves. Only the fundamental mode was present. This package showed evolution of the feed-out seed.
35 Al, 2.2	Strong, fast interface coupling. Strong second harmonic observed in two of the three shots. Feed-out of the perturbation to the ablation front experimentally confirmed with side-on radiography.
84 Al / 10 Be, 2.2	Observed feed-out of the perturbation from beryllium into aluminum. Only the fundamental mode was present. Strong acoustic waves.
32 Al / 10 Be, 2.2	Early time peak observed in fundamental, possibly feed-out of perturbation into the aluminum, but wrong phase. Data implied that harmonics were only in the beryllium and that the Rayleigh-Taylor acted ablatively on the hot surface and classically on the cold surface after feeding-back into the foil.
50 Al, 4.5	Package moved from weak to strong interface coupling. Rayleigh-Taylor vortex pairs dominated package evolution, displacing the Richtmyer-Meshkov vortex pairs.
35 Al, 4.5	Data showed much lower amplitude perturbations than computationally predicted for times after the pulse was off.

The results of this work suggest that greater thickness during the implosion may be part of the reason why beryllium capsules are superior to plastic. The larger density jump between the fuel and ablator in beryllium probably did not have as much of an effect as the thickness in reducing the feed-out. Most importantly, feed-out has been computationally and experimentally demonstrated to couple perturbations on the cold surface of a radiatively driven foil with the Rayleigh-Taylor instability on the ablation surface. From this, one can assume that it will also couple the large DT ice perturbations in ICF capsules to the Rayleigh-Taylor instability on the ablation surface. Such coupling will require either further reduction in the ice perturbation amplitudes or design of feed-out resistant capsules, such as the beryllium capsule.

Some comments will now be made in regard to what work remains to be done. The highest priority needs to be feed-out calculations in the NIF parameter space. Preliminary work suggests that feed-out on NIF may be quite different from NOVA.

Better experiments could be performed in order to quantitatively determine how thickness affects feed-out. The packages proposed would be composed of an aluminum ablator and beryllium payload, with a perturbation on the cold, beryllium surface. Using face-on radiography, one could look at packages with different thicknesses of beryllium, but the same total thickness. The pulse should be short so that only the Richtmyer-Meshkov instability would be induced. The amplitude of the feed-out seed could be observed as it moved toward the ablation

surface at different positions in the package. The reduction in perturbation amplitude with position could be recorded.

Perhaps one could determine if the Rayleigh-Taylor instability was generating harmonics on the cold surface using thin packages with a beryllium ablator and aluminum payload. This would confirm that the Rayleigh-Taylor instability was acting as an ablative instability on the hot surface and as a classical instability on the cold surface. A perturbation could be placed on the hot or cold surface, but preferably the cold surface so data could be compared to the data presented here.

Although probably not of interest to the ICF community, experiments exploring different aspects of interface coupling would be of scientific interest. Freeze-out from Richtmyer-Meshkov and Rayleigh-Taylor interface coupling has had very little experimental investigation. Mikaelian proposed some experiments along these lines [Mikaelian 1996]. Investigations involving Richtmyer-Meshkov interface coupling with a reflected shock instead of a reflected rarefaction wave could be interesting. Perturbations on a shock decay, whereas perturbations on a rarefaction wave do not, so the interface coupling might be weaker when the reflected wave was a shock. In all the experiments in this dissertation, the reflected wave was a rarefaction. There is also the case of total shock transmission at the interface described by Yang. This case might not produce any interface coupling.

Appendix: Details of Individual Shots

Following in Tables 1-7 is a summary of the feed-out experiments performed on NOVA. There was a great deal of information collected on each shot, such as the actual pulse shape generated by the laser and individual beam line energies, but only the more important details are included in the tables below.

Tables 1 and 2 provide information on the packages and the main pulse. The shots are listed in the order in which they were actually fielded, and so the shotnames do not necessarily proceed in order. Each shot had three designation numbers, a shotnumber corresponding to the number of shots the laser had performed up to that point, a target identification number, to designate which package was being shot, and a shotname. For simplicity, only the shotname is provided. The 2.2 ns pulse listed is PS-26, while the 4.5 ns is PS-35. Both of these were described in the introduction. The percent spread in beam energy represents the root mean squared deviation of the individual beam energies from the average. On shot 15, one of the beams had only about a third of the expected energy while another almost did not fire.

Table 3 provides information on the primary diagnostic in SIM 4. The optimal gain for the camera was found by trial and error. The timing pulse delay is the delay time added to the circuit between the NOVA diagnostic trigger and the camera, so the camera calls time zero when the laser starts to fire. This timing was always somewhat in question. The strip timings are delays placed on individual strips after the beginning of the experiment.

Table 4 details problems experienced with each shot and the many lessons learned. The references in the table are to SIM 4 data, unless otherwise specified.

During shots 1 and 2, the first two strips from the X-ray camera were completely saturated. The problem was corrected by placing radiation shields on all the following targets. The addition of a collimator with 50 μm holes also helped reduce noise. In shot 3, a piece of target debris punctured through several filters in the nose cone of the GXI, and almost damaged the microchannel plate. The beryllium filter on SIM 4 was then doubled in thickness to protect the diagnostic.

Another concern was adjustment of the gain on the FXI or GXI. If the gain was too low, the image would not be visible; too high, and the film would be saturated. Trial and error were used to determine the best setting for a given package. On shots 4 and 5, the FXI gain was too low and some data was lost. Low gain was also a problem on shot 20. The FXI was found to be a superior camera to the GXI's and was used exclusively toward the end of the experimental campaign. It did not have as many strips misfire as the GXI's.

Certain backlighters were found to be more desirable than others. Generally, a slightly higher energy backlighter than necessary was initially used to insure that transmission was high enough. Backlighter energy was then slowly decreased to increase the intensity ratio. For the thin packages, Ti was used first, then Sc. For the thick packages, Fe was changed to Mn. The difference in back-

lighters was most noticeable in the side-on shots 11, 12, 9 and 10. Copper was found to be much too dim compared to Fe.

Package thickness became a concern after the 6/96 series of shots. A measure of package thickness was attempted in metrology, and the thicknesses were found to be slightly different than expected. Target fabrication measured the thicknesses on the 8/96 series side-on, but not face-on packages. Shots 11 and 9 were suppose to be with 35 μm thick packages, but they were not, because of fabrication error. Target fabrication suspected there was some kind of systematic error in the process resulting in an additional 4-5 μm thickness for all the packages, at least for the 8/96 shots. The lathe used to machine the packages was much more accurate than the 4-5 μm error. This error could have entered the machining process when the copper substrate was removed from the lathe, placed in the vacuum chamber, then placed back on the lathe. As this systematic error is a suspicion and cannot be confirmed, the requested thicknesses are listed in the tables instead of the suspected thicknesses, with the exception of shots 11 and 9, which were measured.

Streak camera data was lost in shot 20 due to a lead shield falling on the crystal and interfering with X-ray transmission to the streak camera. The shield had previously been Scotch taped by the student to a baffle in the spectrometer in order to reduce noise, but an insufficient amount of tape was used. In future shots the shielding was removed.

In shot 21, the diagnostic alignment was off. For shot 22, we removed

the cap on the FXI, exposing the collimator and pinholes. Alignment of the diagnostic was much easier using the holes in the collimator instead of the featureless face of the cap, but it also ran the risk of damaging the collimator or pinholes more easily. The alignment on shot 22 was good, with no damage to the camera.

Table 5 shows information on the SIM 3 and 6 diagnostics. The terms "TP" and "Cam" delays refer to the timing pulse and camera delays. The camera delay is how long the diagnostic waits from the beginning of the experiment to begin taking pictures. The timing pulse delay is the same as in Table 3. Both diagnostics ran over the same time frame as the backlighter. The GXI strips could be set to the same delays as SIM 4, but they did not have to be. The main purpose of these two diagnostics was to deduce if the backlighter was at fault if there was poor data from SIM 4.

Table 6 contains information on the backlighter element, energy on the backlighter and the energy of the He- α line. Two flat-top pulses were used to drive the backlighter. One was a 3 ns pulse, referred to as (64)*PS1-03, while the 2 ns pulse was (26)*PS1-02. The 2 ns pulse provided more intensity as the laser power was higher. The backlighter beams were turned on 200 ps before the first strip on the X-ray camera fired, providing enough time to generate a plasma on the backlighter disk before pictures were taken.

Data on diagnostic alignment and laser pointing are provided in Table 7. All three diagnostics were pointed at the backlighter. Although SIM 4 was the package diagnostic, it looked at the backlighter through the package. Experience

showed that aligning SIM 3 444 μm above the actual position of the backlighter was more accurate than requesting the exact number. Why this worked is unknown.

Table 1: Packages

Shotname	Date	Thickness (mm)	Face or Side-on
1	4/26/96	86 Al	face
2	4/26/96	84 Al/10 Be	face
3	4/26/96	35 Al	face
4	4/26/96	32 Al/10 Be	face
5	4/26/96	32 Al/10 Be	face
6	6/18/96	86 Al	face
7	6/18/96	86 Al	face
8	6/18/96	35 Al	face
15	8/96	50 Al	face
14	8/96	35 Al	face
13	8/96	35 Al	face
11	8/96	40 Al	side
12	8/96	85 Al	side
9	8/96	41 Al	side
10	8/96	86 Al	side
16	3/97	35 Al	face
17	3/97	35 Al	face
18	3/97	32 Al/10 Be	face
19	3/97	32 Al/10 Be	face
20	3/97	84 Al/10 Be	face
21	3/97	84 Al/10 Be	side
22	3/97	32 Al/10 Be	side

Table 2: Main Pulse

Shotname	Main Pulse Length (ns)	Energy in Hohlräum (kJ)	Requested Energy (kJ)	% Spread in Beam Energy
1	2.2	24.4	25.6	8.33
2	2.2	25.0	25.6	3.72
3	2.2	27.5	25.6	3.54
4	2.2	24.8	25.6	3.32
5	2.2	25.3	25.6	2.50
6	2.2	25.1	24.0	2.49
7	2.2	22.6	24.0	3.03
8	2.2	25.3	24.0	2.93
15	4.5	18.3	24.0	45.77
14	4.5	21.4	24.0	9.69
13	2.2	28.5	24.0	7.00
11	2.2	24.1	24.0	7.13
12	2.2	25.2	24.0	8.62
9	2.2	24.2	24.0	7.45
10	2.2	23.1	24.0	8.23
16	2.2		24.0	
17	2.2	24.2	24.0	12.08
18	2.2	25.3	24.0	2.52
19	2.2	23.1	24.0	1.70
20	2.2		24.0	
21	2.2	25.4	24.0	2.26
22	2.2	24.0	24.0	3.27

Table 3: SIM 4 Diagnostic

Shot-name	SIM 4 Camera & Gain (V)	SIM 4 Filters (mil)	SIM 4 Timing Pulse Delay (ns)	SIM 4 Strip Timings (ns)
1	GXI 3 / -300	11 Be 0.5 Fe	93.80	2.0 / 2.7 / 3.5 / 4.6
2	GXI 3 / -200	11 Be 0.5 Fe	93.80	2.0 / 2.7 / 3.5 / 4.6
3	GXI 3 / -200	11 Be 0.5 Ti	93.80	2.2 / 2.45 / 2.7 / 2.95
4	FXI / +250	21 Be 0.5 Ti	93.80	2.2 / 2.45 / 2.7 / 2.95
5	FXI / +150	21 Be 0.5 Sc	93.80	2.2 / 2.45 / 2.7 / 2.95
6	GXI 2 / -300	21 Be 0.5 Fe	96.20	2.0 / 2.3 / 3.0 / 4.0
7	GXI 2 / -300	21 Be 0.5 Fe	96.20	2.0 / 2.3 / 2.7 / 3.2
8	GXI 2 / -300	21 Be 0.5 Ti	96.20	1.2 / 1.7 / 2.2 / 2.7
15	GXI 3 / -100	21 Be 0.5 V	93.80	4.2 / 4.95 / 5.7 / 6.45
14	GXI 3 / -100	41 Be 0.5 Ti	95.70	2.8 / 3.55 / 4.3 / 5.05
13	GXI 2 / -100	41 Be 0.5 Ti	95.70	1.5 / 1.9 / 2.3 / 2.7
11	GXI 2 / -100	41 Be 0.5 Cu	95.70	1.2 / 1.5 / 1.8 / 2.1
12	GXI 2 / -100	41 Be 0.5 Cu	95.70	2.2 / 2.4 / 3.2 / 3.6
9	GXI 2 / -100	41 Be 0.5 Fe	95.70	1.8 / 2.05 / 2.3 / 2.55
10	GXI 2 / -100	41 Be 0.5 Fe	95.70	3.5 / 3.9 / 4.3 / 5.0
16	FXI / +150	21 Be 0.5 Sc	81.15	1.0 / 1.4 / 1.8 / 2.2
17	FXI / +150	21 Be 0.5 Sc	81.20	1.2 / 1.6 / 2.0 / 2.4
18	FXI / +150	21 Be 0.5 Sc	82.60	1.5 / 1.9 / 2.3 / 2.7
19	FXI / +150	21 Be 0.5 Sc	82.60	1.7 / 2.1 / 2.5 / 2.9
20	FXI / +150	21 Be 0.5 Fe	82.60	2.3 / 2.8 / 3.3 / 3.8
21	FXI / +150	21 Be 0.5 Fe	82.60	2.3 / 2.8 / 3.3 / 3.8
22	FXI / +150	21 Be 0.5 Fe	82.60	1.6 / 2.0 / 2.4 / 2.8

Table 4: Comments on SIM 4 Data

Shotname	Comments on SIM 4 Data and Other Things.
1	No data on strip 1 - did not have batwing shielding.
2	No data on strip 1 - did not have batwing shielding.
3	Strip 3 did not fire. GXI was damaged from target debris.
4	Weak images of the package - gain too low on FXI.
5	Very weak images of the package - gain too low on FXI.
6	Strip 4 did not fire. Forced to use 8 X magnification pinholes with 12 X magnification snout and lost data on all the 1st pinholes.
7	NOVA diagnostic trigger failed to fire. No data.
8	Strip 4 did not fire. Forced to use 8 X magnification pinholes with 12 X magnification snout and lost data on all the 1st pinholes.
15	Laser did not fire properly - low energy. Strips 2 & 4 did not fire.
14	Strips 2 & 4 did not fire.
13	This was the null shot - no perturbations on package.
11	Cu backlighter was dim. Package thickness different from requested.
12	Cu backlighter was dim.
9	Package thickness different from that requested.
10	Shot went well.
16	Did not insert a Be filter built into FXI. Allowed light in and ruined data.
17	Strip 1 did not fire.
18, 19, 22	Shot went well.
20	Gain setting on FXI was too low for thicker packages. No data. Lost data on the streak camera due to lead shielding falling on crystal.
21	Diagnostic alignment off. Could only see cold side of target.

Table 5: SIM 3 and SIM 6

Shot-name	SIM 3 Crystal	SIM 3 Filter (mil)	SIM 3 TP/Cam Delays (ns)	SIM 6 Filter	SIM 6 TP/Cam Delays (ns)
1	PET	11 Be 0.5 Fe	67.70 / 3.3	11 Be 0.5 Fe	47.85 / 2.0
2	PET	11 Be 0.5 Fe	67.70 / 3.3	11 Be 0.5 Fe	47.85 / 2.0
3	RbAP	11 Be 0.5 Ti	67.70 / 3.5	11 Be 0.5 Ti	47.85 / 2.2
4	RbAP	11 Be 0.5 Ti	67.70 / 3.5	11 Be 0.5 Ti	47.85 / 2.2
5	RbAP	11 Be 0.5 Sc	67.70 / 4.5	11 Be 0.5 Sc	47.85 / 2.2
6	PET	11 Be 0.5 Fe	67.70 / 3.3	11 Be + Fe	43.95 / 2.0
7	PET	11 Be 0.5 Fe	67.70 / 3.3	11 Be + Fe	43.95 / 2.0
8	RbAP	11 Be 0.5 Ti	67.70 / 2.0	21 Be	43.95 / 1.2
15	RbAP	0.5 Ti 0.5 V	67.70 / 5.5	41 Be	46.35 / 4.1
14	RbAP	11 Be 0.5 Ti	67.70 / 4.1	41 Be	46.35 / 2.7
13	RbAP	11 Be 0.5 Ti	67.70 / 2.3	41 Be	43.90 / 1.5
11	PET	11 Be 0.5 Cu	67.70 / 2.0	41 Be	43.90 / 1.2
12	PET	11 Be 0.5 Cu	67.70 / 3.0	41 Be	43.90 / 2.2
9	PET	11 Be 0.5 Fe	67.70 / 2.3	Fe	43.90 / 1.8
10	PET	11 Be 0.5 Fe	67.70 / 4.2	Fe	43.90 / 3.5
16	RbAP	11 Be 0.5 Ti	67.74 / 0.8	21 Be	46.35 / 1.0
17	RbAP	11 Be 0.5 Ti	67.74 / 1.0	21 Be	46.35 / 1.2
18	RbAP	11 Be 0.5 Ti	67.74 / 2.3	21 Be	46.35 / 1.2
19	RbAP	11 Be 0.5 Ti	67.74 / 2.3	21 Be	46.35 / 1.7
20	PET	11 Be 0.5 Fe	67.74 / 3.0	21 Be	46.35 / 2.0
21	PET	11 Be 0.5 Fe	67.74 / 3.3	21 Be	46.35 / 2.5
22	PET	11 Be 0.5 Fe	67.74 / 2.6	21 Be	46.35 / 1.6

Table 6: Backlighter

Shot-name	Backlighter & Thickness (μm)	Backlighter He- α (keV)	Backlighter Delay/ Pulse length (ns)	Energy on Backlighter (kJ)
1	18 Fe	6.7	1.8 / 3	8.67
2	25 Fe	6.7	2.0 / 3	8.88
3	25 Ti	4.7	1.5 / 3	9.87
4	25 Ti	4.7	1.5 / 3	8.76
5	Sc	4.3	1.5 / 3	9.16
6	18 Fe	6.7	1.8 / 3	9.15
7	25 Mn	6.2	1.8 / 2	9.65
8	25 Sc	4.3	1.0 / 2	10.82
15	13 V	5.2	4.0 / 3	7.45
14	25 Sc	4.3	2.6 / 3	6.93
13	25 Sc	4.3	1.3 / 2	8.04
11	50 Cu	8.3	1.0 / 2	7.59
12	50 Cu	8.3	2.0 / 2	8.15
9	18 Fe	6.7	1.3 / 2	8.02
10	18 Fe	6.7	2.0 / 2	7.74
16	25 Sc	4.3	0.8 / 2.0	
17	25 Sc	4.3	1.0 / 2.0	9.44
18	16 Sc	4.3	1.3 / 2.0	9.82
19	16 Sc	4.3	1.5 / 2.0	8.93
20	Mn	6.2	2.1 / 2.0	
21	18 Fe	6.7	2.1 / 2.0	9.33
22	18 Fe	6.7	1.4 / 2.0	8.94

Table 7: Laser Beam and Diagnostic Alignment for all Shots

Beam Line or Diagnostic	X (-N/+S) (μm)	Y (-E/+W) (μm)	Z (-Up/ +Down) (μm)	Lens/ Z (- Div/+Con) (μm)
Beams 1,3,5,9	0	1375	0	-1000
Beams 2,4,6,10	0	-1375	0	-1000
Backlighter Beams 7,8 Face- on	3800	0	1236	0
Backlighter Beams 7,8 Side- on	4074	0	404	0
SIM 4 & 6 Face- on	3800	0	1236	N/A
SIM 4 & 6 Side- on	4074	0	404	N/A
SIM 3 Face-on	3800	0	1680	N/A
SIM 3 Side-on	4074	0	848	N/A
Target	0	0	0	N/A

Target rotation was 0 (-CCW/+CW).

Bibliography

- Baltrusaitis, R. M. *et al.* Sept. 1996 "Simulation of Shock Generated Instabilities," Physics of Fluids 8 (9): 2471-2483.
- Bel'kov, S. A. *et al.* 1998 "Simulation of Rayleigh-Taylor Instability Growth Rate of Laser-Accelerated Plane Targets," submitted to Physics of Plasmas.
- Bird, R. B., Stewart, W. E., and Lightfoot, E. N. 1960 Transport Phenomena. John Wiley & Sons New York, NY.
- Byrne, N., Betlach, T., Gittings, M. L., April 28-30, 1992 "RAGE: A 2D Adaptive Grid Eulerian Nonequilibrium Radiation Code," Proceedings of the Defense Nuclear Agency Numerical Methods Symposium.
- Duderstadt, J. and Moses, G. 1982 Inertial Confinement Fusion. New York, NY: John Wiley and Sons, presently out of print.
- Gossard, Earl and Hooke, William. 1975 Waves in the Atmosphere. Elsevier Scientific New York, NY.
- Gittings, M. L., April 28-30, 1992 "SAIC's Adaptive Grid Eulerian Hydrocode," Proceedings of the Defense Nuclear Agency Numerical Methods Symposium
- Haan, S. W. June 1991 "Hydrodynamic Instabilities on ICF Capsules," UCRL-JC-107592. Lawrence Livermore National Laboratories, Livermore, CA.
- Haan, S. W. August 1991 "Weakly Nonlinear Hydrodynamic Instabilities in Inertial Fusion," Physics of Fluids B 3(8): 2349-2355.
- Hoffman, Nelson M. Aug. 1994 "Hydrodynamic Instabilities in Inertial Confinement Fusion," LAUR-94-3945. Los Alamos National Laboratory, Los Alamos, NM.
- Hoffman, Nelson M. 1997 Staff member, MS F663, Los Alamos National Laboratory, Los Alamos, NM 87545. Personal communication.
- Hollowell, D., et al. June 1-5, 1997 "Ablative Rayleigh-Taylor Instability Modeling," Proceedings of the 27th Annual Anomalous Absorption Conference, University of British Columbia, Vancouver, B. C.
- Hogan, W., Bangerter, R., and Kulcinski, G. Sept. 1992 "Energy from Inertial

Fusion," Physics Today 42-50.

Holmes, R. L., Grove, J. W., Sharp, D. H. 1995 "Numerical Investigation of Richtmyer-Meshkov Instability Using Front Tracking," Journal of Fluid Mechanics 301: 51-64.

Krall and Trivelpiece 1986 Principles of Plasma Physics. San Francisco, CA: San Francisco Press, Inc.

Krauser, W. *et al.* 1996 "Ignition Target Design and Robustness Studies for the National Ignition Facility," Physics of Plasmas 3 (5): 2084-2093.

Lindl, J., McCrory, R. L., Cambell, E. M. Sept. 1992 "Progress Toward Ignition and Burn Propagation in Inertial Confinement Fusion," Physics Today 32-40.

Mikaelian, Karnig Oct. 1982 "Rayleigh-Taylor Instabilities in Stratified Fluids," Physical Review A 26 (4): 2140-2158.

Mikaelian, Karnig Sept. 1983 "Time Evolution of Density Perturbations in Accelerating, Stratified Fluids," Physical Review A 28 (3): 1637-1646.

Mikaelian, Karnig Jan. 1985 "Richtmyer-Meshkov Instabilities in Stratified Fluids," Physical Review A 31 (1): 410-419

Mikaelian, Karnig April 1995 "Rayleigh-Taylor and Richtmyer-Meshkov Instabilities in Finite Thickness Fluid Layers," Physics of Fluids 7 (4): 888-890.

Mikaelian, Karnig May 1996 "Numerical Simulation of Richtmyer-Meshkov Instabilities in finite-Thickness Fluid Layers," Physics of Fluids 8 (5): 1269-1291.

Ofer, D. *et al.* 1996 "Modal Model for the Nonlinear Multimode Rayleigh-Taylor Instability," Physics of Plasmas 3(8): 3073-3089.

Ott, Edward, Nov. 1972 "Nonlinear Evolution of the Rayleigh-Taylor Instability of a Thin Layer," Physical Review Letters 29 (21): 1429-1432.

Remington, B. A., *et al.* April 1992 "Large Growth, Planar Rayleigh-Taylor experiments on NOVA," Physics of Fluids B 4 (4): 967-978.

Remington, B. A., *et al.* July 1993 "Laser-Driven Hydrodynamic Instability Experiments," Physics of Fluids B 5 (7): 2589-2595.

- Richtmyer, Robert 1960 "Taylor Instability in Shock Acceleration of Compressible Fluids," Communications on Pure and Applied Mathematics, vol. XIII, 297-319.
- Scannapieco, A. Sept. 1981 "Atmospheric Type Modes in Laser Fusion Targets," Physics of Fluids 24 (9): 1699-1705.
- Schappert, G., *et al.* 1996 "Planar Rayleigh-Taylor Instability Growth in Copper Foils," Proceedings of the 38th Annual Meeting of the Division of Plasma Physics Nov 11-15, Denver, Co.
- Takabe, H., *et al.* 1985 "Self-Consistent Growth Rate of the Rayleigh-Taylor Instability in an Ablatively Accelerating Plasma," Physics of Fluids 28: 3676.
- Weber, S. V., Remington, B. A. *et al.* Nov 1994 "Modeling of NOVA Indirect Drive Rayleigh-Taylor Experiments," Physics of Plasmas 1 (11): 3652-3661.
- Yang, Yumin and Zhang, Qiang May 1993 "General Properties of a Multilayer Stratified Fluids System," Physics of Fluids A 5 (5): 1167-1181.
- Yang, Y., Zhang, Q., Sharp, D. 1994 "Small Amplitude Theory of Richtmyer-Meshkov Instability," Physics of Fluids 6: 1856-1873.
- Youngs, David L. 1984 "Numerical Simulation of Turbulent Mixing by Rayleigh-Taylor Instability," Physica 12D: 32-44.
- Zel'dovich and Razer 1966 Physics of Shock Waves and High Temperature Hydrodynamic Phenomena Volume I, Academic Press, New York, NY.
- Zimmerman, G. B. and Kruer, W. L. 1975 "Numerical Simulation of Laser-Initiated Fusion," Comments on Plasma Physics and Controlled Fusion 2 (2): 51-61.

This report has been reproduced directly from the best available copy.

It is available to DOE and DOE contractors from the Office of Scientific and Technical Information, P.O. Box 62, Oak Ridge, TN 37831. Prices are available from (615) 576-8401.

It is available to the public from the National Technical Information Service, US Department of Commerce, 5285 Port Royal Rd. Springfield, VA 22616.

